ACS APPLIED MATERIALS & INTERFACES
Research Article
Cite This: ACS Appl. Mater. Interfaces 2017, 9, 39657-39671
www.acsami.org

Tannic Acid/Fe^{3+}/Ag Nanofilm Exhibiting Superior Photodynamic and Physical Antibacterial Activity

Ziqiang Xu,[†] Xiuhua Wang,[†] Xiangmei Liu,[†] Zhenduo Cui,[‡] Xianjin Yang,[‡] Kelvin Wai Kwok Yeung,[‖] Jonathan Chiyuen Chung,[§] Paul K. Chu,[§] and Shuilin Wu*[,†,‡]

[†]Hubei Collaborative Innovation Center for Advanced Organic Chemical Materials, Ministry-of-Education Key Laboratory for the Green Preparation and Application of Functional Materials, Hubei Key Laboratory of Polymer Materials, School of Materials Science & Engineering, Hubei University, Wuhan 430062, China

[‡]School of Materials Science & Engineering, Tianjin University, Tianjin 300072, China

[§]Department of Physics and Department of Materials Science and Engineering, City University of Hong Kong, Tat Chee Avenue, Kowloon, Hong Kong 999077, China

[‖]Department of Orthopaedics & Traumatology, Li Ka Shing Faculty of Medicine, The University of Hong Kong, Pokfulam, Hong Kong 999077, China

Supporting Information

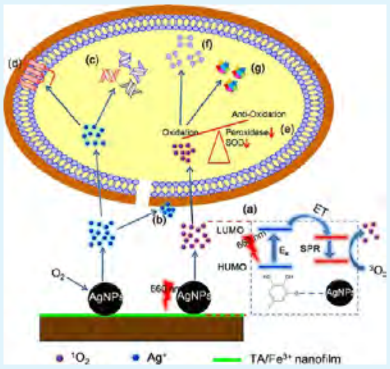

ABSTRACT: Silver nanoparticles (AgNPs) enwrapped in the biologically safe tannic acid (TA)/Fe^{3+} nanofilm are synthesized by an ultrafast, green, simple, and universal method. The physical antibacterial activity and photodynamic antibacterial therapy (PAT) efficacy of the TA/Fe^{3+}/AgNPs nanofilm were investigated for the first time, which exhibited a strong physical antibacterial activity as well as great biocompatibility, through in vitro and in vivo studies. The results disclosed that this hybrid coating could possess high PAT capabilities upon irradiation under a visible light of 660 nm, which is longer than those of previously reported green and blue sensitization light, thus allowing deeper light penetration into biological tissues. Electron spin resonance (ESR) spectra proved that the PAT efficacy of the TA/Fe^{3+}/AgNPs nanofilm was associated with the yields of singlet oxygen ($^1O_2$) under the irradiation of visible light (660 nm). A higher PAT efficiency of 100 and 94% against *Escherichia coli* and *Staphylococcus aureus* could be achieved within 20 min of illumination under 660 nm visible light, whereas the innate physical antibacterial activity of AgNPs could endow the implants with long-term prevention of bacterial infection. The mechanism of PAT may be associated with the formation of oxidative stress and oxidative damage to key biomolecules (proteins and lipids) in bacteria. Our results reveal that the synergistic action of both PAT and physical action of AgNPs in this hybrid nanofilm is an effective way to inactivate bacteria, with minimal side effects.

KEYWORDS: *antibacterial, implants, nanofilm, Ag nanoparticles, photodynamic therapy, infection*

1. INTRODUCTION

Bacterial infections and the ensuing complications often result in the failure of implants used for repair or replacement of hard tissue; such infections are traditionally treated by systemic antibiotic therapy. However, the abuse of antibiotics has been reported to induce bacterial resistance and even multidrug-resistant superbugs.[1] Thus, orthopedists, biomaterial scientists, and engineers have focused their attention on the development of novel artificial implants with inherent antibacterial characteristics.[2]

Varying clinical requirements make it desirable for biomaterials to possess different biological functions.[3] Surface modification is an effective strategy for endowing biomaterials with special surface functions, including enhanced wear-resistance, biocompatibility, osteoconductivity, and osteoinductivity as well as antimicrobial characteristics.[4−6] The surface modifications employed to fabricate self-antibacterial surfaces can be divided into (1) direct impregnation with antibiotics;[7] (2) loading coatings with an inorganic bactericide (e.g., Ag and zinc oxide);[8,9] and (3) loading other antimicrobial agents (e.g., bioactive antibacterial polymer, non-antibiotic organic bactericide, or adhesion-resistant agent) in a matrix bonded to the surface.[10−12]

In particular, coatings containing Ag nanoparticles (AgNPs) deposited on titanium (Ti) have been shown to mitigate implant-related bacterial infection via the release of Ag$^+$. Owing to sustainable release of Ag$^+$, such coatings are stable, effective against a broad spectrum of bacteria and fungi, and have a low propensity to develop bacterial resistance.[13,14] Moreover, human toxicological concerns can be eliminated by adjusting the amount of effective Ag$^+$ released into the extracellular matrix from the implant surface.[15] It has also been reported that

Received: July 23, 2017
Accepted: October 24, 2017
Published: October 24, 2017

DOI: 10.1021/acsami.7b10818

the plasmonical excitation of metal nanoparticles (e.g., Au, Ag, and Pt) forms singlet oxygen ($^1O_2$), which plays an important role in killing microorganisms.[16,17] AgNPs can thus kill bacteria by generating $^1O_2$ under light irradiation, a process termed as photodynamic antibacterial therapy (PAT). It is widely accepted that the AgNPs' size, shape, surface coating, and solution chemistry affect their surface plasmon resonance (SPR) and thus influence the PAT efficacy.[18,19] In fact, PAT has been proven to be a promising strategy to inactivate microorganisms with minimal invasiveness and short cure-time.[20,21]

Various techniques have been implemented to incorporate AgNPs into the near-surface of Ti-based implants, for example, plasma immersion ion implantation (PIII), electrochemical techniques, plasma spraying, and magnetron sputtering, and in situ synthesis.[22] However, most of these methods are time-consuming and require an elaborate apparatus or toxic reagents, consequently hampering wider commercial acceptance.[23−26]

Natural building blocks that can be assembled into functional films on a Ti surface have aroused scientific and technological interests.[27−30] Recently, a simple and rapid strategy has been proposed to deposit nanofilms on different substrates by the coordinated assembly of tannic acid (TA) and Fe^{3+}, which has been recognized to be safe by the U.S. Food and Drug Administration.[31] TA, as a kind of analogue to water-soluble tannin, is a high-molecular-weight ubiquitous natural polyphenol with five ester groups attached to a glucose core via a covalent bond. Metal-chelating is a typical property of TA (like many other polyphenols), and it can be considered as a polydentate ligand for metal coordination. Along with its metal-chelating abilities, derived from the abundant phenolic hydroxyl groups on the gallic acid moieties, these functional groups also endow TA with superior antioxidation and reduction abilities in alkaline environments.[32−34] Herein, a novel, ultrafast, green, simple, and universal method has been developed to fabricate organic−inorganic hybrid coatings (TA/Fe^{3+}/AgNPs), that is, AgNPs enwrapped in the biocompatible TA/Fe^{3+} nanofilm.

Our in vitro and in vivo studies proved that the as-prepared hybrid coatings not only possessed superior physical antibacterial activity (i.e., Ag^+ release-killing) and good biocompatibility but also showed better and rapid PAT efficacy due to the generation of $^1O_2$ during 660 nm visible-light illumination. Although light with a longer wavelength penetrates tissues more deeply and possesses less toxicity than conventional green and blue light,[35] activation of oxygen on AgNPs with such a long wavelength has hitherto rarely been reported. Our demonstration of a long sensitization wavelength will expand the clinical use of AgNPs in PAT. Such biocompatible coatings with a robust physical and PAT efficiency can be achieved through this ultrafast, green, simple route at an ambient temperature without special equipment or toxic reagents, which makes this method preferable to most others.

2. EXPERIMENTAL SECTION

2.1. Preparation of Samples. *2.1.1. Preparation of TA/Fe^{3+} Nanofilm.* Medical grade Ti plates with a diameter of 6 mm and a thickness of 2 mm were utilized as the starting materials on which the nanofilm was deposited. First, the Ti plates were mechanically ground using SiC sand papers of 240, 400, 800, and 1200 grits successively and then ultrasonically cleaned in ethanol and deionized water. Prior to the deposition of the TA/Fe^{3+} nanofilm, the Ti plates were dried in air.

The Ti plates were soaked in 20 mL of deionized water. Then 200 μL of 40 mg/mL TA (Aladdin Reagent Co., China) was added into the above deionized water under vigorous magnetic stirring. The solution was stirred for 1 min, and 200 μL of 6 mg/mL $FeCl_3$ (Aladdin Reagent Co., China) was subsequently added dropwise into the solution under vigorous magnetic stirring. The mixture turned blue immediately. Finally, the pH value of the mixture was adjusted to 8.0 by adding 1 mol/L NaOH dropwise. Then, the substrates were rinsed with deionized water. This deposition process was repeated 10 times, leading to the formation of the TA/Fe^{3+} nanofilm on the surface of Ti plates.

2.1.2. Preparation of TA/Fe^{3+}/AgNPs Nanofilm. Silver ammonia solution [$Ag(NH_3)_2OH$] was prepared through dropwise addition of ammonia (10 wt %) to $AgNO_3$ (SIGMA Co., USA), until the brown precipitate was completely dissolved and the final concentration of $Ag(NH_3)_2OH$ was 250 mmol/L. Then, different volumes (200, 400 μL) of freshly prepared $Ag(NH_3)_2OH$ solution were added dropwise into 10 mL of deionized water with the TA/Fe^{3+}-capped Ti plates at the bottom. The surface color of Ti plates turned black within 1 min. The mixture was stirred for further 30 min to obtain stable and uniform AgNPs on the surface of Ti plates. Finally, these modified Ti plates were rinsed with deionized water and then dried in air. Two types of samples with $Ag(NH_3)_2OH$ having a final concentration of about 5 and 10 mmol/L were denoted as TA/Fe^{3+}/AgNPs-5 and TA/Fe^{3+}/AgNPs-10, respectively.

2.2. Characterization. The surface morphologies of samples were examined by scanning electronic microscopy (SEM, JSM-6510LV, JEOL, Japan). Transmission electron microscopy (TEM) images were recorded on a Tecnai G20 electron microscope (FEI, USA). Field emission scanning electron microscopy (FE-SEM) was employed to obtain a high-resolution image of the surface morphologies (JSM7100F, JEOL, Japan). Inductively coupled plasma atomic emission spectrometry (ICP-AES) was carried out on an Optima 8000 (PerkinElmer, USA) spectrometer to analyze the concentration of the released ions. The total content of Ag deposited on Ti was detected by ICP-AES after digestion using concentrated HNO_3. Raman spectra were obtained with an inVia Reflex spectrometer (Renishaw, UK), and the 632.8 nm line of an air-cooled He/Ne laser was used as the excitation source. X-ray photoelectron spectroscopy (XPS) was carried out on an ESCALAB 250Xi instrument (Thermo Scientific, USA) to study the element states and depth distribution of the elements in the nanofilm. The nanoindentation and nanoscratch were performed by a TI-950 Nano DMA II/III transducer (Hysitron USA).

2.3. Contact Angle. The contact angles of different samples were measured at an ambient temperature by a contact angle instrument (Powereach jc2000D1Zhong-Cheng Digital, China), with deionized water as the test medium. A drop of distilled water (5 μL) was placed on the sample surface, and the contact angle was recorded by an optical microscope. The values are the average of three drops at three different positions on the surface of different samples.

2.4. Antibacterial Study. Both *Escherichia coli* (*E. coli*, ATCC 8099) and *Staphylococcus aureus* (*S. aureus*, ATCC 25923) were applied to evaluate the antibacterial activity of the different Ti plates (MP-Ti, TA/Fe^{3+}, TA/Fe^{3+}/AgNPs-5, and TA/Fe^{3+}/AgNPs-10) through inhibition zone assays and the spread plate method in a standard Luria Bertani (LB) medium at 37 °C.

2.4.1. Inhibition Zones Assay. The zones of inhibition were measured by placing different Ti plates on LB agar plates seeded with bacteria. Namely, the bacteria suspensions were first diluted with melted LB agar plates to 1×10^7 cfu/mL. Then, they were poured onto watch glasses. All Ti plates were placed on the surface of the LB agar plates and incubated at 37 °C for 24 h with *E. coli* and *S. aureus*. Finally, the inhibition zones appeared around the samples with superior physical antibacterial activity.

2.4.2. Spread Plate Assay. Aliquots of diluted bacterial suspensions (1×10^7 cfu/mL) were mixed with different samples. Then, they were divided into three groups (cocultured for 24 h in the dark, cocultured for 20 min in the dark, and illuminated for 20 min by 660 nm visible light). Then, the bacterial suspension was further diluted 100 times by LB. Finally, 10 μL of the diluted bacterial suspension was added onto a solid medium by the spread plate method and cultured at 37 °C for 24 h.

The bacterial ratio can be quantified through counting the number of colonies on the plates recorded by the digital camera, which is determined according to the eq 1

$$\text{Bactericidal ratio } (\%) = \frac{\text{cfu}_{\text{control}} - \text{cfu}_{\text{sample}}}{\text{cfu}_{\text{control}}} \quad (1)$$

2.4.3. Bacterial Morphology Assay. SEM was applied to study the morphology and early adhesion behavior of *E. coli* and *S. aureus* on Ti plates. After the bacterial suspension was treated according to the above procedures, the bacteria on Ti were fixed with 2.5% glutaraldehyde for 2 h, rinsed with phosphate-buffered saline (PBS) three times, dehydrated with a series of ethanol solutions (30, 50, 70, 90, and 100 v/v %) successively for 15 min each, and dried in air for SEM observation.[36]

2.4.4. PAT Mechanism of TA/Fe^{3+}/AgNPs. The bacteria cells were treated according to the above procedures. Then, the peroxidase and superoxide dismutase (SOD) activities were detected by a peroxidase detection kit and a SOD detection kit (mlBio China). Moreover, the content of protein carbonyl was detected by the reaction with 2,4-dinitrophenylhydrazine, and products of lipid peroxidation were measured by the thiobarbituric reacting substances (TBARS) assay, according to previous methods.[37]

2.5. In Vitro Biocompatibility Evaluation. *2.5.1. MTT Assay.* The different Ti plates, including mechanically polished Ti plates (MP-Ti), TA/Fe^{3+}, TA/Fe^{3+}/AgNPs-5, and TA/Fe^{3+}/AgNPs-10, were laid in a 48-well plate. The cell suspensions were diluted and seeded into the 48-well plate. After incubation for different periods (1, 3, and 7 days), 3-(4,5-dimethylthiazol-2-yl)-2,5-diphenyltetrazolium bromide (MTT; 0.5 mg/mL) was added, and the cells were further incubated with MTT for an additional 4 h until a purple precipitate was visible. Then, 300 μL of dimethyl sulfoxide was added to completely dissolve the crystals via vibration for 10 min. Finally, a microplate reader was used to measure the absorption at 490 nm (SpectraMax I3 MD USA).

2.5.2. Cell Adhesion and Spreading Study. The cells were seeded onto the Ti plates with different coatings in a 48-well plate. After incubating for a certain amount of time (1 or 7 days), the seeded cells were rinsed with PBS (pH 7.4) three times and then fixed with 4% formaldehyde (Sinopharm Chemical Reagent Co., China) solution in PBS (pH 7.4) for 10 min at an ambient temperature, followed by rinsing with PBS three times. Then, the cytoskeletal actin of the cells was labeled with fluorescein isothiocyanate (FITC)−phalloidin (100 nmol/L, Yisen, Shanghai, China), and the nuclei were stained with 4′,6-diamidino-2-phenylindole (DAPI, 100 nmol/L, Yisen, Shanghai, China) successively. Finally, the cells were analyzed via fluorescence microscopy (IX73, Olympus, USA).

2.5.3. Alkaline Phosphatase (ALP) Activity. After incubation with different Ti plates in a 48-well plate for different periods (3, 7, and 14 days), the cultured cells on the Ti plates were lysed by 200 μL of 1% Triton X-100 (Sinopharm Chemical Reagent Co., China) dissolved in PBS and then stored at 37 °C for 1 h. Then, they were centrifuged (1100 rpm) for 10 min, and 30 μL of the supernatant was transferred into a 96-well plate. Finally, the intracellular ALP activity was detected via an ALP detection kit (Jiancheng Biotech, China).

2.6. In Vivo Experiments. To investigate the in vivo antibacterial and histological effects, the prepared samples were implanted into the subcutaneous tissues of rats. The model-specific pathogen-free Wistar male mice of 200 g were purchased from Google biological corporation (Wuhan, China). The mice were divided into two groups as follows: MP-Ti and TA/Fe^{3+}/AgNPs-10, with each group containing four mice.

After implantation of the samples into the subcutaneous tissues, 20 μL of *S. aureus* with a concentration of 1×10^7 cfu/mL was inoculated into the place of the implants. Then, the surgical sites of one mouse in each group was irradiated with 660 nm visible light for 20 min and euthanized at 1 day. Meanwhile, the other six mice in the absence of light were euthanized two mice at a time at 1, 4, and 7 days. Finally, the implants were removed, and the bacteria in the body fluid of surgical sites were counted after dilutions of 400 times through the spread plate method.

The surrounding tissues contacting the implants were extracted from each mouse and fixed with 4% formaldehyde solution for 24 h. Then, the tissue was processed for routine histology and cut into 4 μm thicker transverse sections. Finally, the sections from each mouse were stained with hematoxylin−eosin (H&E).

3. RESULTS AND DISCUSSION

3.1. Formation Mechanism of TA/Fe^{3+}/AgNPs Nanofilm. The procedure for preparing the TA/Fe^{3+} nanofilm and organic−inorganic hybrid coatings (TA/Fe^{3+}/AgNPs) on Ti plates is shown in Scheme 1a. In this process, the plant polyphenol TA, a natural and readily available substance, and Fe^{3+} were chosen as the organic polymer ligand and the inorganic cross-linker, respectively. The molecular structure of TA is given in Scheme 1b. The surface of MP-Ti could be easily encapsulated with a coordination-based nanofilm by successive additions of TA and Fe^{3+} to an aqueous solution containing MP-Ti producing a brown color on the Ti plate within several seconds (Scheme 1a). Each Fe^{3+} coordinates with three galloyl groups of TA, leading to the formation of a cross-linked nanofilm on the MP-Ti surface.[31] As TA and Fe^{3+} were added, the water turned blue immediately, stemming from the formation of the TA/Fe^{3+} complex. The nanofilm is formed almost instantaneously, and the mixing time has negligible effects on the color under the standard conditions.

Scheme 1. Schematic Illustration of the Formation of the TA/Fe^{3+}/AgNPs Nanofilm on the Ti Implant via Self-Assembly and In Situ Reduction Method (a), Chemical Structures of TA (b), and Schematic Illustration of the Formation Processes of the TA/Fe^{3+} Nanofilm on the Ti Surface (c) as well as the Reduction Mechanism of TA Transforming Ag(NH$_3$)$_2$$^+$ to Metallic Ag (d)

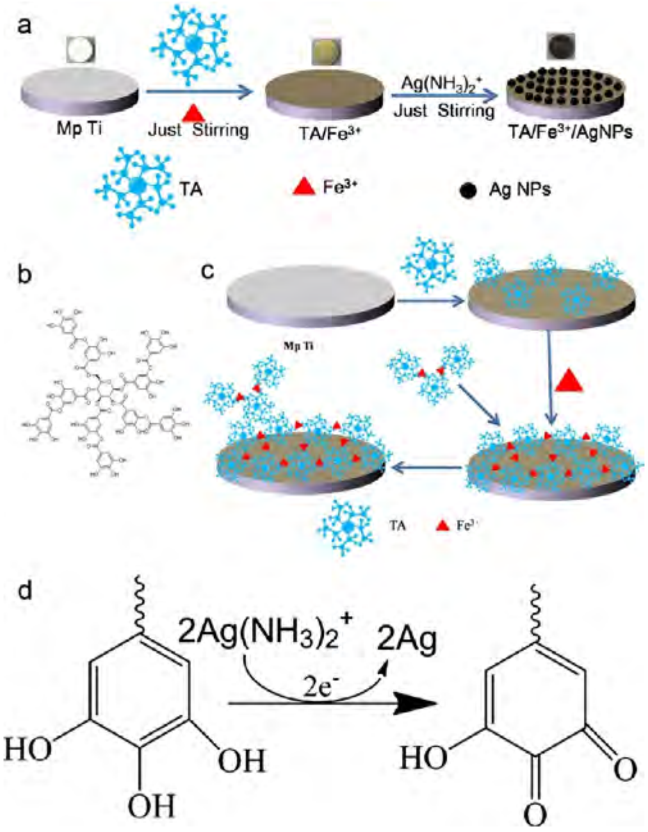

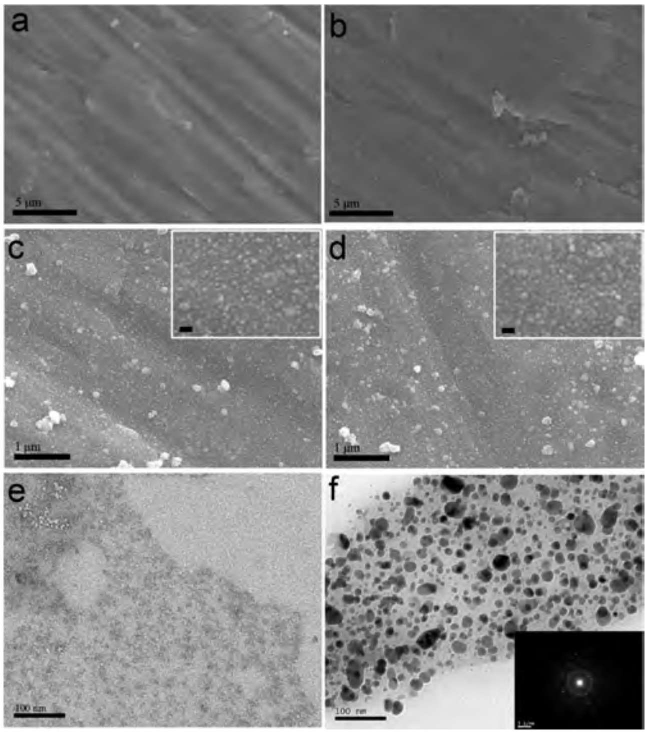

Figure 1. Surface morphologies: (a) SEM images of MP-Ti, (b) SEM images of TA/Fe^{3+}, (c) SEM images of TA/Fe^{3+}/AgNPs-5 (inset: high-resolution SEM images of TA/Fe^{3+}/AgNPs-5, scale bar: 100 nm), (d) SEM images of TA/Fe^{3+}/AgNPs-10 (inset: high-resolution SEM images of TA/Fe^{3+}/AgNPs-10, scale bar: 100 nm), (e) TEM images of the TA/Fe^{3+} nanofilm, and (f) TEM images of the AgNP-decorated TA/Fe^{3+} nanofilm (inset: SAED pattern of AgNPs).

The mechanism of the formation of the TA/Fe^{3+} nanofilm on the Ti surface is as follows. Generally, as a derivative of marine protein adhesives, TA possesses catechol moieties that exhibit good absorption abilities on various surfaces, including Ti.[38] Therefore, free TA first adheres onto the surface of Ti, and TA is subsequently cross-linked by coordinating with Fe^{3+} to form an octahedral complex. The excess Fe^{3+} absorbs more TA and a small TA/Fe^{3+} complex from the suspension to the surface of the previously formed TA/Fe^{3+} nanofilm (Scheme 1c). This formation process is completed within several seconds.

By taking advantage of the coordination and moderate reducing properties of TA under a mildly alkaline environment,[32−34] AgNPs were successfully in situ deposited onto the surface of the TA/Fe^{3+} nanofilm. The TA/Fe^{3+}-modified Ti plates turned black within several minutes (Scheme 1a). The possible formation mechanism of AgNPs, reduction of $Ag(NH_3)_2^+$ by TA, is shown in Scheme 1d. In TA, only 10 pairs of *o*-dihydroxyphenyl were able to convert phenolic hydroxyl to quinones and donate electrons to $Ag(NH_3)_2^+$ via the redox reactions. Meanwhile, the remaining phenolic hydroxyl stabilizes the AgNPs under alkaline conditions through the coordination reaction.

3.2. Characterization of TA/Fe^{3+}/AgNPs Nanofilm. The surface morphology of the TA/Fe^{3+} nanofilm capped Ti was similar to that of MP-Ti, indicating that the TA/Fe^{3+} nanofilm was very thin and did not affect the original topography of the substrate (Figure 1a,b). Only small particles could be observed, which could possibly stem from the small TA/Fe^{3+} complex formed in the solution. The flat and thin surface morphology was also clearly observed in the FE-SEM images (Figure S1).

However, when AgNPs were enwrapped in the TA/Fe^{3+} nanofilm by the reduction of $Ag(NH_3)_2^+$, the surface of MP-Ti became rough (Figure 1c,d); this was further investigated by FE-SEM. As shown in the inset of the images of Figure 1c,d, the AgNPs covered by the TA/Fe^{3+} nanofilm uniformly were quasi-spherical and monodispersed. The size of AgNPs in TA/Fe^{3+}/AgNPs-5 and TA/Fe^{3+}/AgNPs-10 was in the range of 12−42 and 20−49 nm, respectively, which was smaller than that prepared by PIII.[39] Moreover, more agglomerates and larger

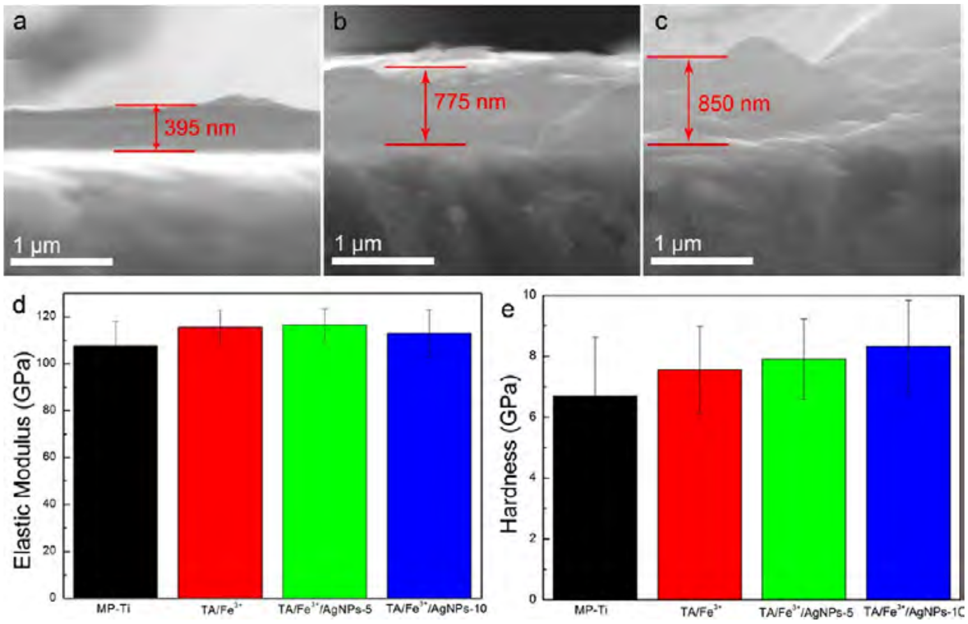

Figure 2. Cross-sectional images of (a) TA/Fe^{3+}, (b) TA/Fe^{3+}/AgNPs-5, and (c) TA/Fe^{3+}/AgNPs-10; (d) elastic modulus (GPa) and (e) hardness (GPa) of various samples.

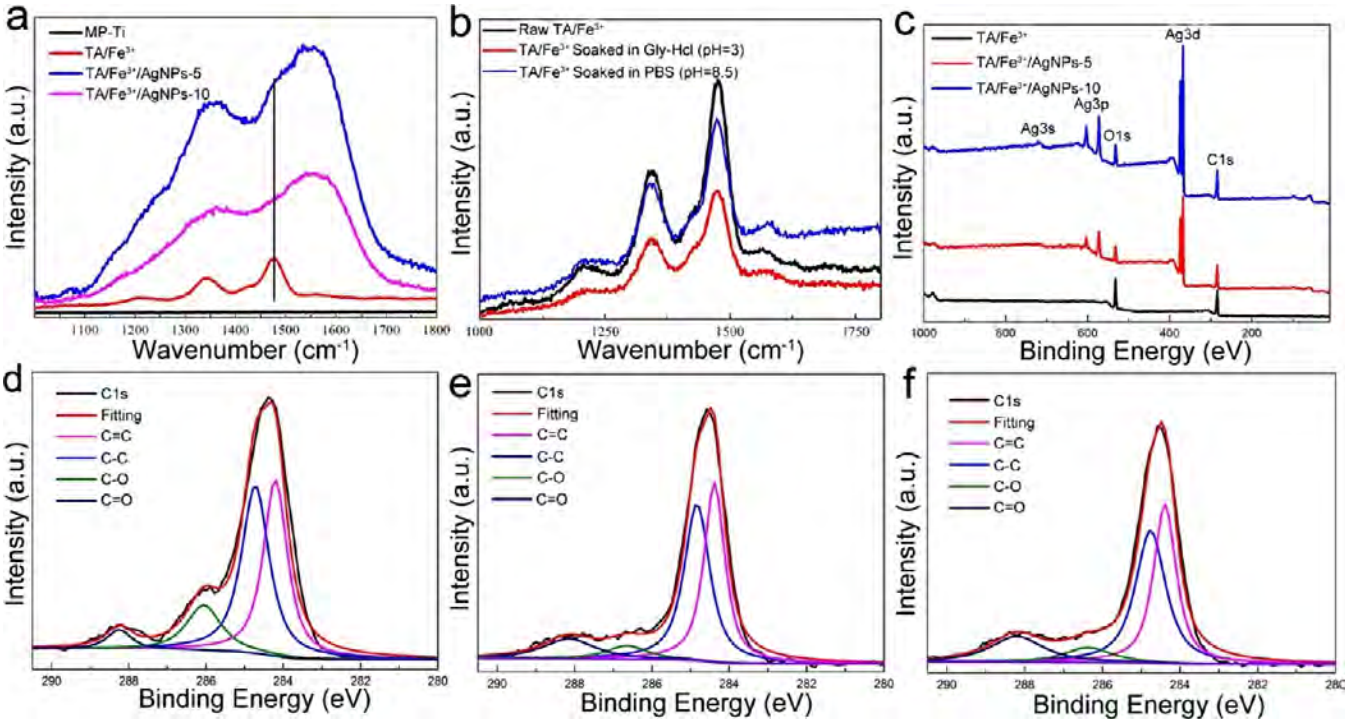

Figure 3. Raman spectra of different samples: (a) Raman spectra of MP-Ti, TA/Fe^{3+}, TA/Fe^{3+}/AgNPs-5, and TA/Fe^{3+}/AgNPs-10; (b) Raman spectra of TA/Fe^{3+} before and after incubation in Gly-HCl (pH = 3) or PBS (pH = 8.5) for 3 days; (c) XPS spectra of TA/Fe^{3+}, TA/Fe^{3+}/AgNPs-5, and TA/Fe^{3+}/AgNPs-10; high-resolution C 1s XPS spectra of (d) TA/Fe^{3+}, (e) TA/Fe^{3+}/AgNPs-5, and (f) A/Fe^{3+}/AgNPs-10.

Table 1. Atomic Percentage of Different Elements in TA/Fe^{3+}, TA/Fe^{3+}/AgNPs-5, and TA/Fe^{3+}/AgNPs-10

	sample	C 1s	O 1s	Fe 2p	Ag 3d
atomic %	TA/Fe^{3+}	69.31	29.82	0.87	
	TA/Fe^{3+}/AgNPs-5	64.7	19.25		14.82
	TA/Fe^{3+}/AgNPs-10	60.91	18.99		18.59

Table 2. Area Percentages of Deconvoluted Peaks in the Total C 1s XPS Spectra of TA/Fe^{3+}, TA/Fe^{3+}/AgNPs-5, and TA/Fe^{3+}/AgNPs-10

	sample	C=C	C−C	C−O	C=O
area %	TA/Fe^{3+}	38.8	42.5	14.3	4.4
	Ag/TA/Fe^{3+}-5	37.9	42.0	10.3	9.8
	Ag/TA/Fe^{3+}-10	37.4	41.6	7.1	13.9

Table 3. Ag Release Kinetics Parameters Obtained from the Fick's Law According to Peppas Model

sample	*k*	*n*	R^2
TA/Fe^{3+}/AgNPs-5	0.507	0.359	0.988
TA/Fe^{3+}/AgNPs-10	0.796	0.323	0.986

clusters were observed on TA/Fe^{3+}/AgNPs-10, which may be attributed to the much higher concentrations of $Ag(NH_3)_2^+$.

The morphology of the different surface coatings on MP-Ti was also examined by TEM. As shown in Figure 1e, the thin TA/Fe^{3+} nanofilm was decorated with some gray dots, which may be assigned to the TA/Fe^{3+} complex. Figure 1f also shows that the quasi-spherical AgNPs were uniformly enwrapped in the TA/Fe^{3+} nanofilm and that the size of most of the AgNPs was below 50 nm. These results were in accordance with the SEM examination. The as-prepared AgNPs were polycrystalline

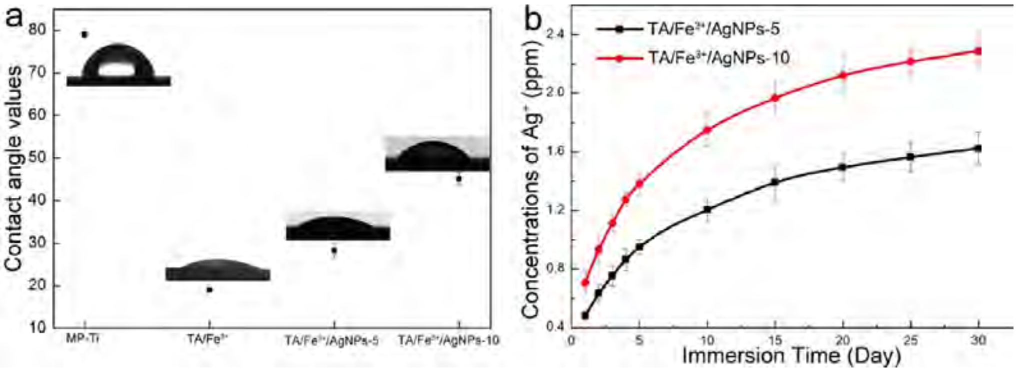

Figure 4. (a) Surface wettability of different samples. The images of water droplets lying on Ti plates with different coatings and the corresponding contact angle values. (b) Ag^+ release from TA/Fe^{3+}/AgNPs-5 and TA/Fe^{3+}/AgNPs-10 in PBS.

DOI: 10.1021/acsami.7b10818
ACS Appl. Mater. Interfaces 2017, 9, 39657−39671

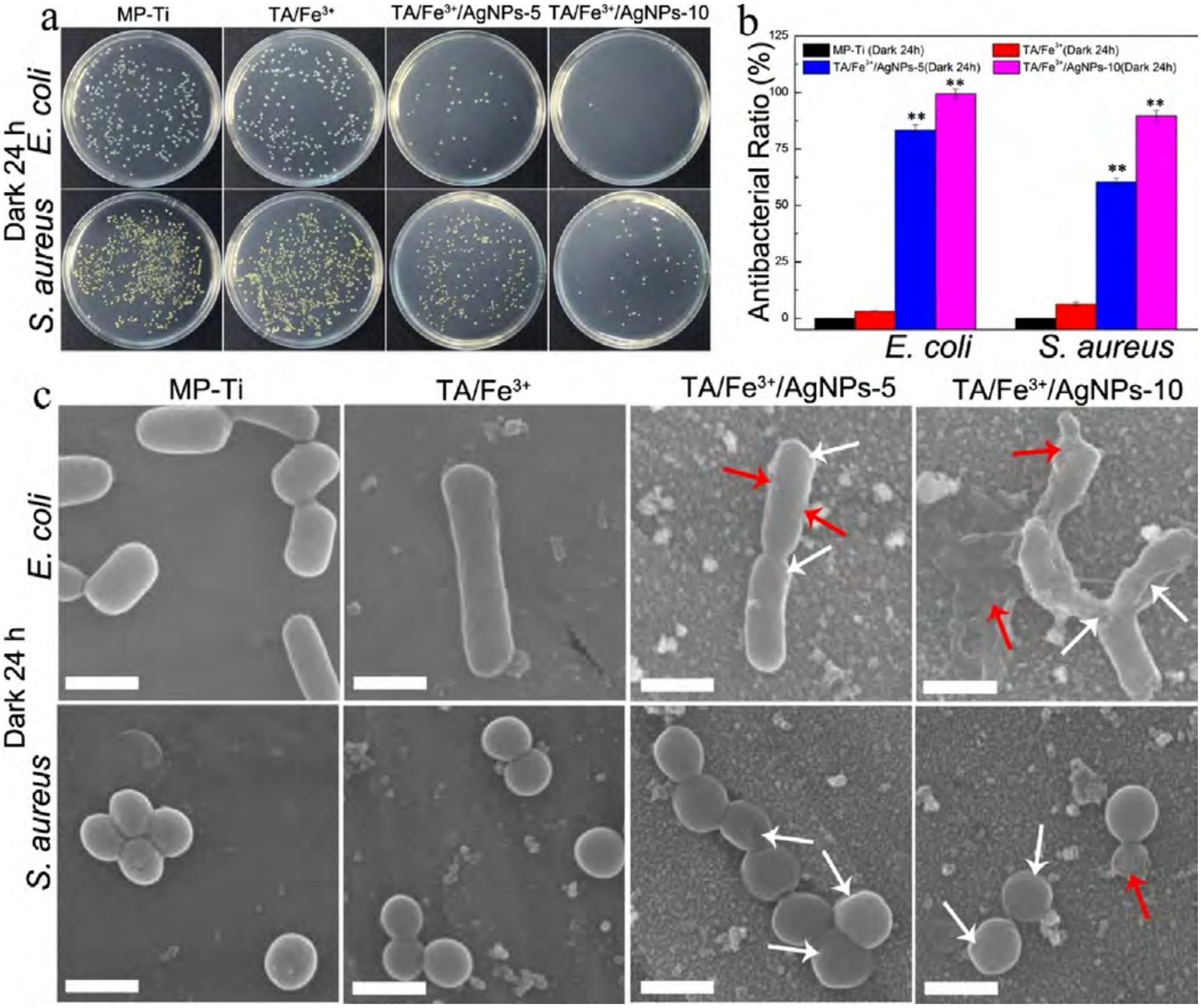

Figure 5. (a) Plate samples showing colonies of *E. coli* and *S. aureus* incubated with different samples under dark for 20 min. (b) Antibacterial ratio of different samples measured according to the number of colonies in the different samples. $^{**}P < 0.01$ vs MP-Ti as the control. (c) Morphologies of *E. coli* and *S. aureus* attached on MP-Ti, TA/Fe^{3+}, TA/Fe^{3+}/AgNPs-5, and TA/Fe^{3+}/AgNPs-10 after incubating for 24 h in the dark (scale bar: 1 μm).

in nature, which could be proven by the selected area electron diffraction (SAED) pattern of the AgNPs. The SAED pattern of AgNPs showed obvious diffraction rings derived from the random orientation of the lattice faces (inset image in Figure 1f). The illumination of the TA/Fe^{3+}/AgNPs-10 hybrid nanofilm with 660 nm visible light does not induce any morphological changes in the AgNPs, which indicates the high-resistant stability of the synthesized AgNPs to light irradiation (Figure S2)

The morphology of the nanofilm was also studied by the cross-sectional images (Figure 2a−c). It was very obvious that the TA/Fe^{3+} nanofilm was very flat, and its thickness was around 395 nm. When the AgNPs were deposited onto the nanofilm, the TA/Fe^{3+}/AgNPs nanofilm became much rougher, and the thickness increased to 775 nm for TA/Fe^{3+}/AgNPs-5 and 800 nm for TA/Fe^{3+}/AgNPs-10. All these results demonstrated that the TA/Fe^{3+} nanofilm was very thin and that the AgNPs were successfully enwrapped in this nanofilm. The energy-dispersive spectrometry (EDS) mapping proved the existence of the nanofilm on the surface of Ti plates and the uniform distribution of C, O, Ag, and Fe elements, further demonstrating the successful deposition of the TA/Fe^{3+}/AgNPs nanofilm on Ti (Figure S3). The hardness (*H*) and Young's modulus (Er) of the nanofilm were characterized by the nanoindentation (Figure 2d,e). Although the Er of both TA/Fe^{3+} and TA/Fe^{3+}/AgNPs were very close to that of MP-Ti, compared with MP-Ti, *H* increased obviously in the sequence of TA/Fe^{3+}, TA/Fe^{3+}/AgNPs-5, and TA/Fe^{3+}/AgNPs-10. Furthermore, the binding forces of the nanofilm were determined by the nanoscratch assay (Figure S4). The average binding force of TA/Fe^{3+} was in the range of 2.7−4.7 mN, which was comparable with that of MP-Ti (3−5.3 mN), indicating that the nanofilm was adhesive and flexible. Thus, the TA/Fe^{3+} nanofilm and Ag incorporation did not change the mechanical property of MP-Ti, that is, TA/Fe^{3+}-modified Ti was mechanically compatible for orthopedic application. The fluctuations of the measured lateral force should be ascribed to the variation in the surface roughness.

The presence of Ag on the Ti surface could also be verified by EDS. As shown in Figure S5, the TA/Fe^{3+}-capped Ti plates

Scheme 2. Schematic Illustration of the Mechanism of Physical Antibacterial Activity of TA/Fe^{3+}/AgNPs: (a) Interfere with the Membrane Permeability by Ag^+, (b) Making DNA Condensed, and (c) Inhibiting Respiratory Enzymes. (d) Schematic Illustration of the Mechanism of Activation of Oxygen to Form $^1O_2$. Schematic Diagram of the Mechanism of PAT of TA/Fe^{3+}/AgNPs: (e) Interfere with the Membrane Integrity by $^1O_2$, (f) Downregulate the Activities of Two Typical Antioxidative Enzymes (SOD and Peroxidase), (g) Cause Lipoperoxidation, and (h) Induce Protein Oxidative Damage

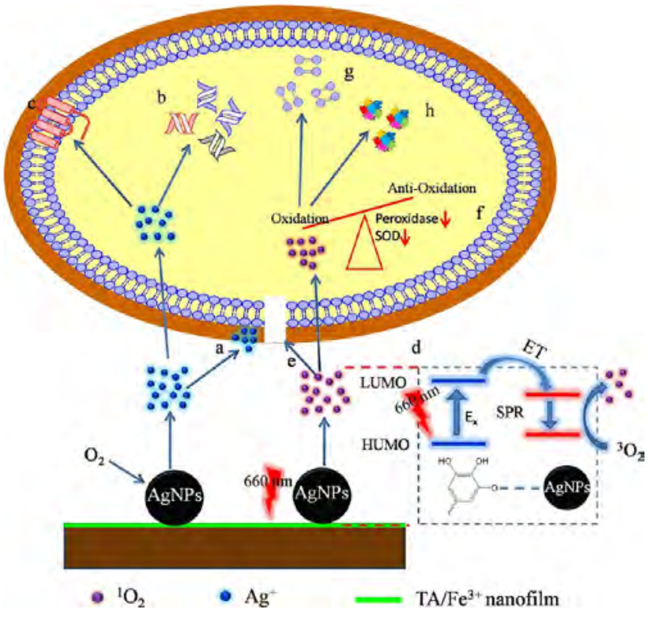

were mainly composed of Ti, C, O, and Fe. The largest signal obtained from the substrate was that of Ti. However, for the samples decorated with AgNPs, an extra, obvious, and intense peak derived from Ag was observed; whereas the Ag peak on TA/Fe^{3+}/AgNPs-10 was much higher than that on TA/Fe^{3+}/AgNPs-5, indicating that the AgNPs were successfully enwrapped within the TA/Fe^{3+} nanofilm and the content of Ag on TA/Fe^{3+}/AgNPs-10 was much higher. The total content of Ag determined by ICP-AES was 49.45 and 76.80 $\mu g/cm^2$ on TA/Fe^{3+}/AgNPs-5 and TA/Fe^{3+}/AgNPs-10, respectively. This content is much higher than the previous reported value by ultraviolet (UV) light reduction strategy,[24] which indicated the high deposition efficiency of this proposed route.

Raman spectra shown in Figure 3a display two obvious peaks at 1346 and 1474 cm^{-1}, which are attributed to the stretch vibration of the C−O bond and the stretch vibration of the C═C ring in TA.[40] However, when AgNPs were deposited on the Ti surface, the intensity of the two Raman peaks of TA increased by about 3-fold and 5-fold; this enhancement was driven by the surface-enhanced Raman scattering (SERS) effect of AgNPs. This phenomenon further indirectly confirmed that AgNPs were successfully enwrapped in the TA/Fe^{3+} nanofilm. The mechanism of SERS is still under debate; however, there are two main enhancement mechanisms that have been widely accepted as possibly contributing to the overall effect, namely, the charge-transfer mechanism and the electromagnetic mechanism.[41] However, the band ascribed to the stretching vibration of C−O shifted from 1346 to 1360 cm^{-1}, which might also be associated with the SERS effect of AgNPs. Interestingly, the peak at 1474 cm^{-1} disappeared, and a new band at 1549 cm^{-1} appeared. We speculated that the transformation mentioned above (phenolic hydroxyl to quinones) as well as the SERS effect contributed to the shifting for this band.

The stability of the nanofilm under acidic and alkaline conditions was also studied. When the TA/Fe^{3+} nanofilm-capped Ti was soaked in Gly-HCl solution (pH = 3) or PBS (pH = 8.5) for at least 3 days, the surface color of TA/Fe^{3+} remained brown, indicating that the nanofilm was highly stable under these two conditions. The continued presence of the TA/Fe^{3+} nanofilm after soaking in Gly-HCl or PBS was also verified via Raman spectra (Figure 3b). The two typical peaks were still observed in the Raman spectra of the TA/Fe^{3+} nanofilm when incubated in Gly-HCl solution or PBS. However, the intensity of the two peaks decreased for both the conditions, indicating that part of the TA/Fe^{3+} nanofilm degraded or dissolved into the surrounding medium under these conditions. Between the two conditions, the peak intensity for the TA/Fe^{3+} nanofilm in PBS (pH = 8.5) was much larger, implying better stability of the TA/Fe^{3+} nanofilm under alkaline conditions.

The XPS spectra of the TA/Fe^{3+} nanofilm showed two peaks centered at 284.3 and 532.1 eV, which could be assigned to C 1s and O 1s, respectively (Figure 3c). The presence of Fe^{3+} was confirmed by its high-resolution spectra (Figure S6). As for the TA/Fe^{3+}/AgNPs hybrid coatings, several peaks associated with Ag were observed, which further confirmed that Ag was successfully enwrapped within the TA/Fe^{3+} nanofilm (Figure 3c). In addition, the chemical states of Ag were determined by typical Ag 3d spectra (Figure S7). Both TA/Fe^{3+}/AgNPs-5 and TA/Fe^{3+}/AgNPs-10 showed the peaks of Ag $3d_{3/2}$ and Ag $3d_{5/2}$ at 374.2 and 368.2 eV, respectively, which were identical to Ag(0).[42] The relative amounts of different elements in the three coatings are listed in Table 1. It should be noted that the Fe content could not be determined for TA/Fe^{3+}/AgNPs hybrid coatings as the binding energy of Ag 3s overlapped with that of Fe 2p, and the signal of Ag 3s was much stronger (Figure S6). The XPS depth profile showed that Ag mainly existed on the surface of the nanofilm, and its content decreased gradually with the increase in deepness. This situation is the same for the element O. On the contrary, the content of C continued to increase with the increase in deepness (Figure S8).

To confirm the reduction mechanism mentioned above, the typical C 1s spectra of the three nanofilms were analyzed (Figure 3d−f). All three C 1s could be fitted into four types of carbon-related groups, and their relative contents are given in Table 2. The contents of both C═C and C−C groups remained constant, whereas the relative contents of both C−O and C═O changed as soon as AgNPs were introduced onto the TA/Fe^{3+} nanofilm. The ratio of C═O to C−O for TA/Fe^{3+}/AgNPs-10 was much higher than that for TA/Fe^{3+}/AgNPs-5, especially for TA/Fe^{3+}. This result further confirmed the aforementioned redox reaction.

3.3. Wettability Studies.

In biological systems, the surface wettability of materials plays an important role in bacterial/cell adhesion, spreading, and protein absorption on implants.[24] The surface wettability of materials can be determined via contact angle measurement. The images of water drops lying on Ti plates with different coatings and their corresponding contact angle values are shown in Figure 4a. Compared with MP-Ti, all other coatings showed improved surface hydrophilicity. In detail, the measured contact angle of the MP-Ti surface was about 79° while the TA/Fe^{3+} nanofilm was fully hydrophilic

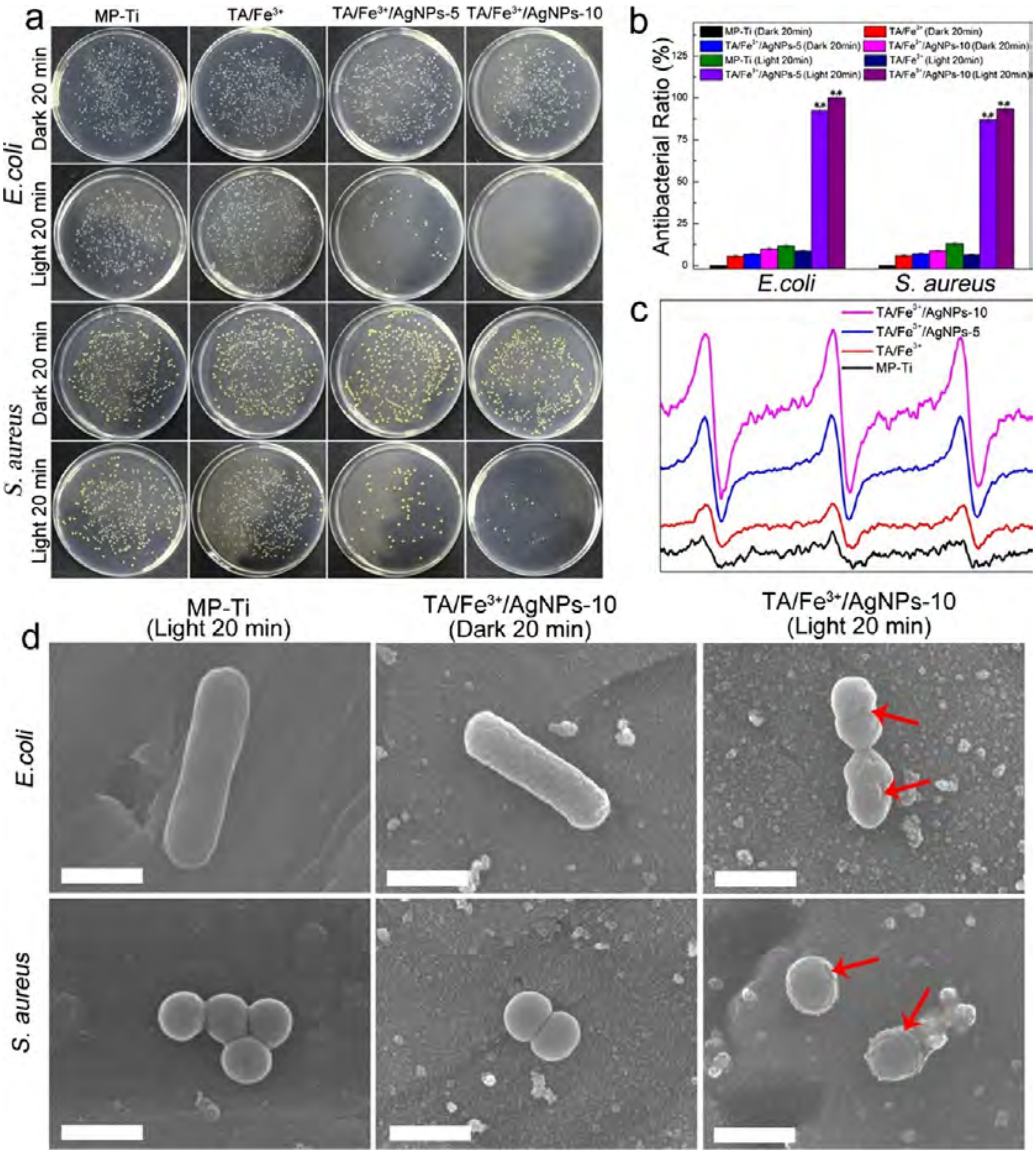

Figure 6. (a) Plate samples showing colonies of *E. coli* and *S. aureus* incubated with different samples under illumination of 660 nm visible light for 20 min or in the dark. (b) Antibacterial ratio of different samples determined according to the number of colonies in the plate samples $^{**}P < 0.01$ vs the Ti group as the control. (c) ESR signals of $^1O_2$ obtained upon irradiation of different samples for 20 min in the presence of TEMP. (d) Morphologies of *E. coli* and *S. aureus* seeded on MP-Ti and TA/Fe^{3+}/AgNPs-10 under the illumination of 660 nm visible light for 20 min (scale bar: 1 μm).

with water drops nearly completely spreading on the surface. The obvious improvement of surface hydrophilicity for the TA/Fe^{3+} nanofilm was mainly derived from the inherent superior hydrophilicity of TA molecules. The surface hydrophilicity of the TA/Fe^{3+} nanofilm decreased obviously as the AgNPs were incorporated onto the surface, and higher concentrations of $Ag(NH_3)_2^+$ further decreased the surface hydrophilicity. However, compared with MP-Ti, the as-prepared nanofilm was still sufficiently hydrophilic. As the surface hydrophilicity benefits the adhesion of osteoblasts on implants, the hydrophilic nature of the hybrid nanofilms will favor the bone cell adhesion on Ti plates.[43]

3.4. Ag^+ Release in PBS.

Figure 4b shows the Ag^+ leaching behavior from TA/Fe^{3+}/AgNPs hybrid coatings in PBS. In the early stage (0−5 days), the release rate of Ag^+ from TA/Fe^{3+}/AgNPs hybrid coatings was rapid, and it slowed down gradually as the immersion time increased (5−30 days), indicating long-term release durability. Furthermore, the concentration of the released Ag^+ continued to increase after 30 days. The final concentrations of Ag^+ released from TA/Fe^{3+}/AgNPs-5 and TA/Fe^{3+}/AgNPs-10 were 1.6 and 2.3 mg/L, respectively, which were high enough to inhibit bacterial adhesion and growth.[44] Moreover, the amount of Ag^+ released from TA/Fe^{3+}/AgNPs hybrid coatings increased with the increase in the initial $Ag(NH_3)_2^+$ concentration.

The mechanism of Ag^+ release from the TA/Fe^{3+}/AgNPs hybrid nanofilm can be analyzed by the Fick's law via fitting the releasing curve according to the simple Peppas model (eq 2)[45]

$$Q = \frac{M_t}{M_e} = kt^n \tag{2}$$

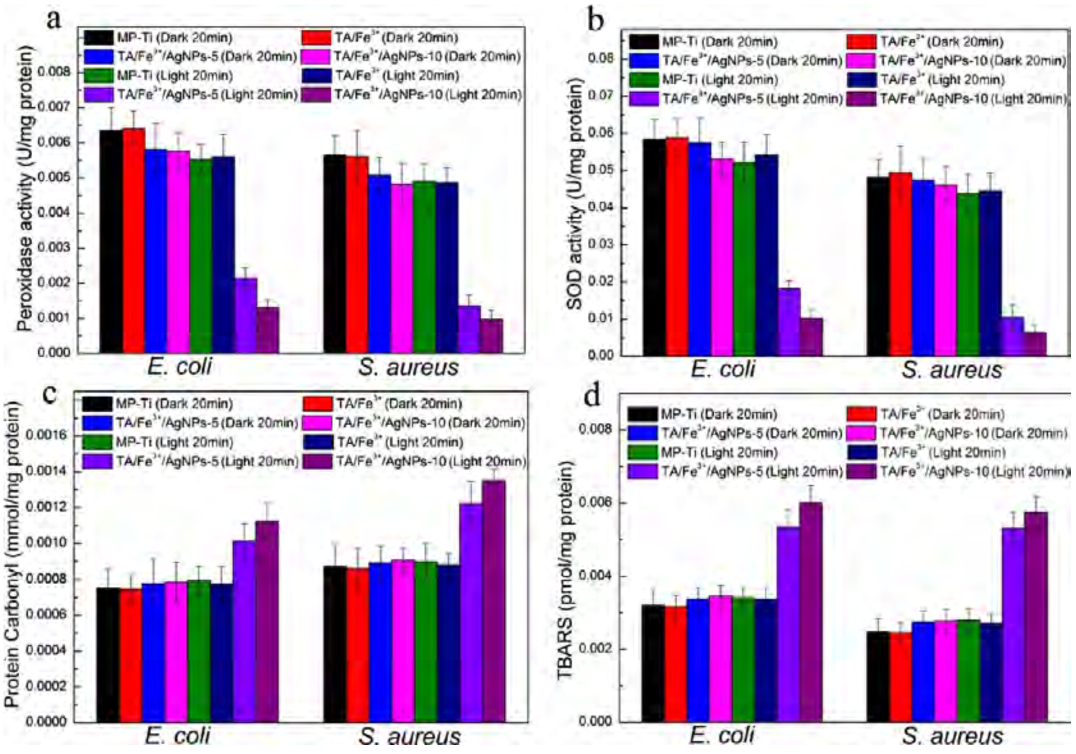

Figure 7. Effects of PAT on activities of antioxidative enzymes in *E. coli* and *S. aureus*: (a) peroxidase and (b) SOD. PAT-induced oxidative damage to proteins and lipids in *E. coli* and *S. aureus*: (c) effects of PAT on the level of protein carbonyl; (d) effects of PAT on the level of TBARS (mean ± SD, $n = 3$).

where M_t/M_e is the fraction of Ag^+ released at time (day) and Ag^+ released at equilibrium, k represents the kinetic constant related to the drug release, and n is the diffusion exponent illustrating the release mechanism. In this regard, when $n < 0.5$, the Fickian-type release dominates, whereas for $0.5 < n < 1$, the non-Fickian type release dominates. The releasing curves equal to 1 indicates the zero order type release. Both the n values for the two kinds of hybrid nanofilms are lower than 0.5, which indicates that the Ag^+ release is dominated by the Fickian type (Table 3). The release of Ag^+ from the TA/Fe^{3+}/AgNPs may occur in two steps. First, the dissolution of AgNPs in the solution can occur via oxidation of the metallic silver into Ag^+, and Ag^+ was coordinated by TA to form Ag^+/TA hybrid coatings; seecond, the diffusion of Ag^+ into the surrounding medium was carried out through the Fickian mechanism.[46]

3.5. Physical Antibacterial Assay.

As shown in Figure 5a, compared with MP-Ti, a negligible difference was observed for the bacterial suspension cocultured with TA/Fe^{3+} for 24 h. However, the bacterial colony formation was almost completely inhibited when the bacterial suspension was cocultured with TA/Fe^{3+}/AgNPs nanofilms for 24 h, especially for TA/Fe^{3+}/AgNPs-10. The bacteria-killing efficacy of TA/Fe^{3+}/AgNPs-5 was about 83 and 60% against *E. coli* and *S. aureus*, respectively, whereas the corresponding efficiency of TA/Fe^{3+}/AgNPs-10 increased to 100 and 90%, respectively (Figure 5b).

The disc diffusion method was further applied to investigate the antibacterial efficacy of different coatings (Figure S9). It was very obvious that MP-Ti did not show any inhibition zone, and the TA/Fe^{3+} nanofilm also did not exhibit any obvious inhibition zone. However, the TA/Fe^{3+}/AgNPs nanofilms showed inhibition zones clearly against *E. coli* and *S. aureus*. The diameter of the inhibition zones increased with increase in the initial $Ag(NH_3)_2^+$ content. These two results indicated that the AgNP-decorated nanofilms possessed superior antibacterial activity, and a higher initial Ag content could produce better antibacterial activity. This further suggested that the antibacterial activity of TA/Fe^{3+}/AgNPs nanofilms may be derived from the released Ag^+. In other words, only the leached Ag^+ could diffuse into the surrounding agar plates to inhibit bacterial growth and form inhibition zones.

The influence of AgNP-decorated nanofilms on the bacterial morphology and membrane integrity (*E. coli* and *S. aureus*) was studied by SEM. MP-Ti was applied as a control (Figure 5c). The *E. coli* seeded onto MP-Ti primarily showed the typical rod shape and was kept intact by binary fission. Those seeded onto TA/Fe^{3+} also displayed the regular rod shape. However, the membrane of the bacteria on TA/Fe^{3+}/AgNPs-5 became much rougher, and irregular shapes could be observed. Additionally, portions of the membrane were shrunk (white arrows), and several parts were completely broken (red arrows). As for bacteria on TA/Fe^{3+}/AgNPs-10, though the shape of *E. coli* could be identified, the shrinkage level of the cell membrane was much more serious (white arrows), and the regular shape could hardly be observed. In addition, part of the cell membrane was completely destroyed, and the spreading membrane could be observed (red arrows). Likewise, *S. aureus* on MP-Ti and TA/Fe^{3+} nanofilm exhibited a spherical shape with smooth and integrated cell membranes. A few cells with a slight shrinkage of membranes were also observed. As expected, more shrunken cells were observed in *S. aureus* on TA/Fe^{3+}/AgNPs-5, and the shrinkage level was more serious (white arrows). In addition, bacteria lysis (red arrows) and cell shrinkage (white arrows) were observed on TA/Fe^{3+}/AgNPs-10. These results implied that the AgNP-decorated nanofilms killed the two bacterial species by disrupting the cell membrane

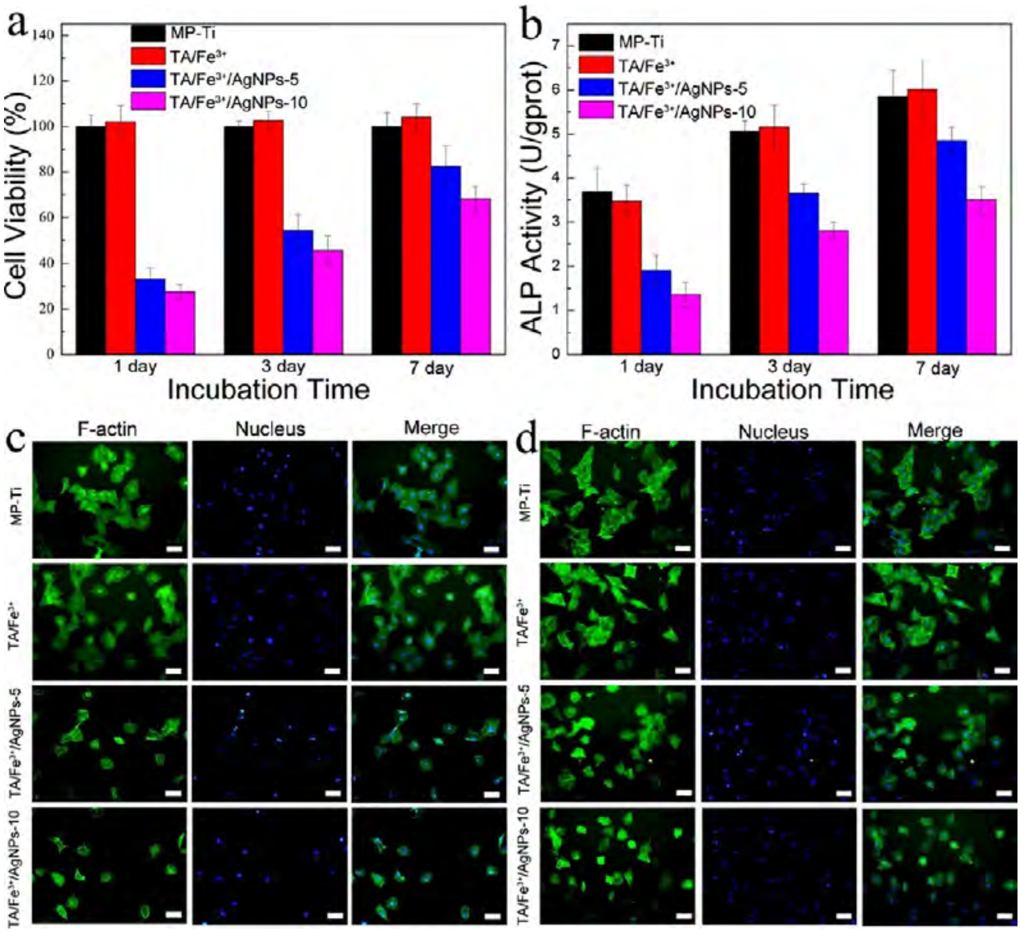

Figure 8. Effects of various coatings on the cell viability (a) and ALP activity (b) of MC3T3 cell of mice (mean ± SD, $n = 3$). Fluorescent images of MC3T3 cells cultured on different samples for (c) 1 day and (d) 7 days (scale bar: 50 μm).

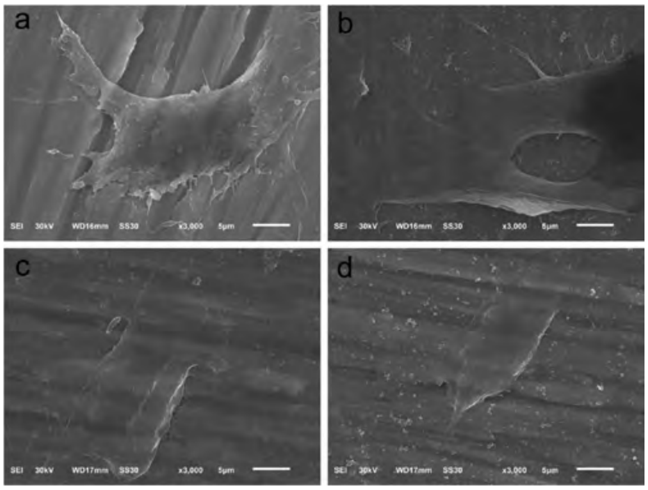

Figure 9. Cell morphologies of MC3T3 cells cultured for 7 days observed by SEM on (a) MP-Ti, (b) TA/Fe^{3+}, (c) TA/Fe^{3+}/AgNPs-5, and (d) TA/Fe^{3+}/AgNPs-10.

integrity and that TA/Fe^{3+}/AgNPs-10 exhibited a better ability than TA/Fe^{3+}/AgNPs-5 in killing the bacteria.

Xiu et al. suggested that the antibacterial effects of AgNPs were derived from the release of Ag^+ alone, whereas the surface chemistry, morphology, and size of the AgNPs could contribute to the antibacterial activity through affecting the release rate and bioavailability of Ag^+.[47] In this work, the mechanism of physical antibacterial activity of TA/Fe^{3+}/AgNPs nanofilms may be associated with the release of Ag^+ from AgNPs, and then, Ag^+ displays superior physical antibacterial activity by interfering with the membrane permeability, inhibiting respiratory enzymes and making DNA molecules condensed (Scheme 2a−c).[48]

3.6. PAT Assay. The efficacy of PAT of nanofilms was investigated by irradiating the bacterial suspension by visible light (660 nm) for 20 min (Figure 6a). Similar trends could be observed for *E. coli* and *S. aureus*. A superior antibacterial effect was observed only from the AgNP-decorated nanofilms irradiated by 660 nm visible light. The other samples displayed little antibacterial effects on the bacterial colonies, compared with MP-Ti cultured with the bacterial suspension in the absence of light. The antibacterial ratio of TA/Fe^{3+}/AgNPs-5 illuminated by 660 nm visible light was 92 and 87% against *E. coli* and *S. aureus*, respectively, whereas the corresponding values of TA/Fe^{3+}/AgNPs-10 was nearly 100 and 94%, respectively, which is very much preferable to TA/Fe^{3+}/AgNPs-5 (Figure 6b). These AgNP-decorated nanofilms in the dark also showed little influence on the growth of bacteria, which may attribute to the fact that the contact time between the bacteria and AgNPs is not long enough to exert an obvious antibacterial effect of Ag^+.

The PAT efficacy of TA/Fe^{3+}/AgNPs nanofilms might be associated with the generation of $^1O_2$, which could be proven by the electron spin resonance (ESR) with 2,2,6,6-tetramethylpiperidine (TEMP) as $^1O_2$ trappers (Figure 6c). Although a

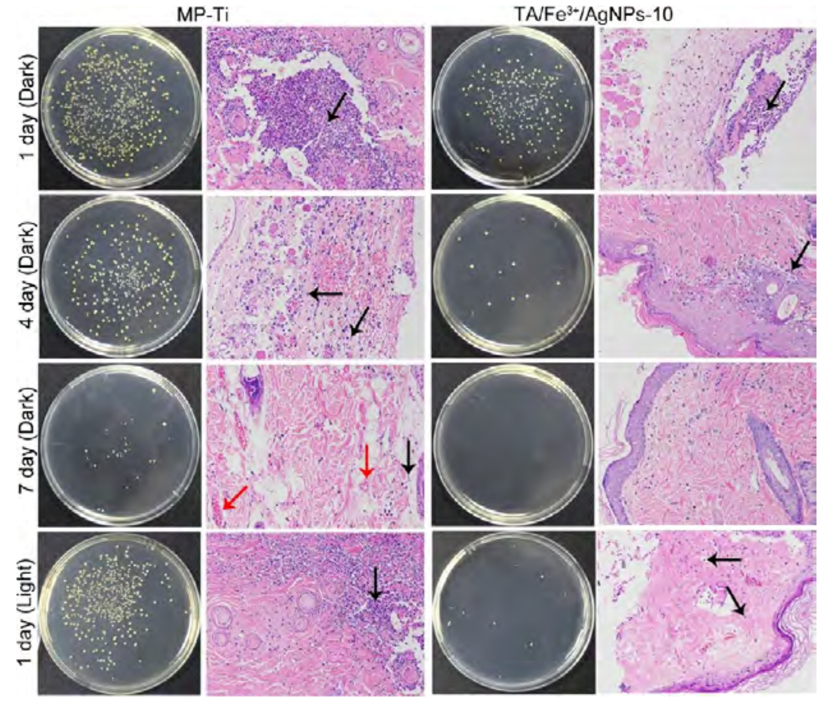

Figure 10. Plates for the colonies of *S. aureus*, which were taken out from the subcutaneous infection mode. Representative histological images of tissues adherent to different samples after H&E staining.

characteristic $^1O_2$-induced signal, 2,2,6,6-tetramethylpiperidine-1-oxyl, was observed in the ESR spectra of MP-Ti because of the small amount of TiO_2 formed during mechanical polishing, the signal intensity observed from TA/Fe^{3+}/AgNPs was far larger than that obtained from MP-Ti, implying that the $^1O_2$ could be effectively produced during illumination with 660 nm visible light. The illumination of the other AgNPs without the assistance of TA/Fe^{3+} does not induce any obvious PAT activity (Figure S10), which proves the key role of the TA/Fe^{3+} nanofilm in the PAT irradiated by 660 nm visible light.

Vankayala et al. reported an unprecedented observation that $^1O_2$ can be formed by direct sensitization of metallic nanoparticles (Ag, Au, and Pt) assisted by their SPR absorption bands.[16] However, a negligible amount of $^1O_2$ is formed by the AgNPs when excited by light with a wavelength longer than 520 nm.[16] So, maybe there is another mechanism that shifts the irradiation light to a longer wavelength. Creutz et al. proposed a photosensitization mechanism induced by surface modifiers. That is, the irradiation in the typical absorption bands results in the transfer of electrons from the surface modifier (ligand) to the SPR bands of metallic NPs. Generally, a ligand should be a good electron donor (catechol).[49] Because TA, a component of the TA/Fe^{3+}/AgNPs nanofilm, is one of the typical derivatives of catechol and the TA/Fe^{3+} nanofilm exhibited a broad absorption band between 400 and 700 nm (Figure S11), TA/Fe^{3+} first absorbed the visible light with a longer wavelength (660 nm), and electrons were transferred from TA/Fe^{3+} to the SPR bands of AgNPs to activate oxygen and generate the $^1O_2$ (Scheme 2d). Meanwhile, the ESR signal generated by TA/Fe^{3+}/AgNPs-5 is much weaker, which indicated that more AgNPs would boost the generation of $^1O_2$. It should be noted that the TA/Fe^{3+} nanofilm could not sensitize the formation of $^1O_2$ efficiently in the absence of AgNPs (Figure 6c), which implied the key role of AgNPs in the origin of $^1O_2$.

We also compared the PAT efficiency of the TA/Fe^{3+}/AgNPs nanofilm by near-infrared light (NIR, 808 nm). As the absorption of TA/Fe^{3+} at NIR is very low (Figure S11), TA/Fe^{3+}/AgNPs hybrid nanofilms cannot be sensitized by the NIR light to form $^1O_2$. Then, the illumination of the TA/Fe^{3+}/AgNPs hybrid nanofilm by NIR light (808 nm) failed to kill both bacteria effectively (Figure S12).

The morphologies of bacteria seeded on different samples irradiated by 660 nm visible light were also studied (Figure 6d). Compared with MP-Ti in the dark environment, two types of bacteria attached on MP-Ti showed regular morphologies. Moreover, though the surface of the bacteria became a little rougher after coculturing with TA/Fe^{3+}/AgNPs-10, their growth and metabolism activity remained well, which could be proven by the images of the spread plate (Figure 6a). However, obvious irregular shapes of the bacteria on TA/Fe^{3+}/AgNPs-10 irradiated by visible light (660 nm) could be observed. Almost all cellular membranes were shrunk for the two types of bacteria, and the membrane of *S. aureus* was even totally destroyed (red arrow). So, one mechanism of PAT may be associated with the interference of membrane integrity (Scheme 2e).

In general, biological aerobic bacteria possess an antioxidative system that can protect the cells from oxidative damage caused by various reactive oxygen species (ROS), including $^1O_2$. Hence, the response of the bacterial antioxidative system to the $^1O_2$ should be the main mechanism of PAT.[37] First, activities of two typical antioxidative enzymes for PAT-treated bacteria were determined. These two enzymes include SOD and peroxidase, which play an important role in the ROS elimination. As shown in Figure 7a,b, only AgNP-decorated nanofilms irradiated by 660 nm visible light decreased the activities of both antioxidative enzymes for the two bacteria, resulting in the accumulation of $^1O_2$ in bacteria.

As soon as the $^1O_2$ is accumulated in the cells, the biomolecules, such as proteins and lipids, will be damaged by the oxidative stress, which can be employed as an indicator of appearance of oxidative stress.[50] In this work, protein carbonyl contents and lipid peroxide, which can be used as biomarkers for protein oxidative damage and lipoperoxidation, were applied to evaluate the levels of oxidative damage to proteins and lipids (Figure 7c,d). It was evident that Ag-enwrapped nanofilms illuminated by 660 nm visible light could increase the level of lipoperoxidation and protein oxidative damage, whereas the proteins were more sensitive to the oxidative stress induced by PAT.

On the basis of the above results, the mechanism of PAT may be associated with the interference of membrane integrity, formation of oxidative stress, and oxidative damage to key biomolecules (proteins and lipids) in bacteria (Scheme 2e−h).

3.7. In Vitro Biocompatibility. Cell viability on different coatings after incubation for 1, 3, and 7 days was investigated by the MTT assay. As shown in Figure 8a, compared with the control group (MP-Ti), a slightly higher cell viability is observed for cells seeded onto TA/Fe^{3+}, indicating the good biocompatibility of the TA/Fe^{3+} nanofilm. Although the survival rates of cells incubated on the AgNP-decorated nanofilms for 1 day are relatively low (33 and 27% for TA/Fe^{3+}/AgNPs-5 and TA/Fe^{3+}/AgNPs-10, respectively), the cell viability increased as the incubation time increased from 1 to 7 days. After 7 days of incubation, the survival rates increased to 82 and 68% for TA/Fe^{3+}/AgNPs-5 and TA/Fe^{3+}/AgNPs-10, respectively, demonstrating the superior biocompatibility of the AgNP-decorated nanofilms. The obvious increase in the cell viability may be attributed to the coordination between the released Ag^+ and partially dissolved TA, which reduced the bioavailability of Ag^+ and ultimately alleviated the toxicity of the coatings. This result is in good agreement with our previous work.[51]

ALP activity is another important indicator that can reflect the osteogenic differentiation levels and promote bone mineral formation.[52] It was very obvious that the ALP activity of cells seeded onto MP-Ti increased with increasing incubation time and that the TA/Fe^{3+} nanofilm exhibited negligible influence on osteogenic differentiation (Figure 8b). However, the AgNP-decorated nanofilms exhibited an obvious negative effect on the ALP activity when being incubated for 3 days, and this situation improved when the incubation time was increased from 3 to 14 days. The negative effect of TA/Fe^{3+}/AgNPs-10 was much stronger than that of TA/Fe^{3+}/AgNPs-5. These results confirmed that the AgNP-decorated nanofilms displayed good biocompatibility, especially as the incubation time increased.

The first stage of cell−implant interaction is determined by the initial adhesion and spreading behavior of cells on the interface, which is regulated by the signaling pathways. The quality of this phase affects the ability of cells to proliferate and differentiate.[53] Thus, the initial cell adhesion and spreading behavior could be visualized via staining of F-actin and nucleus with FITC−phalloidin and DAPI, respectively. As shown in Figure 8c, cells seeded onto MP-Ti for 1 day display superior adhesion with a spreading morphology, and the spreading morphology of cells on TA/Fe^{3+} was comparable to that on MP-Ti. A similar expression of F-actin filaments and filopodia could be observed in the two types of samples. In addition, elongated morphologies were also observed in both samples, which caused cytoskeletal tension and stress on the implant surface. Oh et al. reported that the obvious elongation of stem cells could induce cytoskeletal stress and differentiation of cells.[54] This result further indicated the biocompatibility of the TA/Fe^{3+} nanofilm. However, the relative amount of cells adhered and the sizes of the cells on the AgNP-decorated nanofilm were much smaller. Even though the expression of F-actin filaments and filopodia on the AgNP-decorated nanofilm was worse than that on both MP-Ti and TA/Fe^{3+}, moderate spreading and adhesion could still be observed. Moreover, slight filopodia extensions were apparent on the AgNP-decorated nanofilm. After culturing for 7 days and in comparison with the sample cultured for 1 day, discernible differences in morphologies and cell quantities were observed (Figure 8d). In addition, the relative number of cells adhering onto the AgNP-decorated nanofilm increased, and it was comparable to those cultured on MP-Ti and TA/Fe^{3+}. These results were in accordance with the MTT assay, showing the good biocompatibility of the AgNP-decorated nanofilm.

Furthermore, the surface morphology of cells seeded onto different samples was observed via SEM. As shown in Figure 9, the cells were well-attached, well-spread, and viable on all samples. The cells seeded on MP-Ti spread well and showed elongated morphologies and a large number of filopodia. The cell growth on TA/Fe^{3+} exhibited elongated morphologies and a large number of filopodia. Moreover, it could be observed that the clustered cells covered the samples with connections among them through filopodia. Although the cells spread well on the AgNP-decorated nanofilm, they displayed polygonal shape, and a little filopodia could be observed, suggesting that the AgNP-decorated nanofilms were biocompatible. The results of fluorescence microscopy and SEM were in accordance with those of the MTT assay, showing that AgNP-decorated nanofilms possessed good biocompatibility.

3.8. In Vivo Assay. Subcutaneous implantation was applied to investigate the in vivo antiinfection and histological effects. The infection status of the wounds was assessed by the bacterial colonies extracted from the tissue fluids spread on the LB agar medium (Figure 10). It was obvious that the bacterial colonies for both groups showed similar trends in a dark environment, that is, the number of colonies decreased obviously with the increase in the implantation time. However, a remarkable difference could be observed in the plates for the mice implanted with TA/Fe^{3+}/AgNPs-10, that is, colony formation was almost completely prevented when TA/Fe^{3+}/AgNPs-10 was implanted into the mice for 4 days. Furthermore, little colonies were observed on the plates cultured with tissue fluids extracted from the mice (1 day) implanted with TA/Fe^{3+}/AgNPs-10 and illuminated by visible light (660 nm) after surgery. As for the MP-Ti group irradiated by 660 nm visible light, the number of colonies was much larger than the experimental groups and comparable with that of MP-Ti in the dark. These results confirmed that the AgNP-decorated nanofilms possessed superior in vivo antibacterial efficacy through the synergistic action of PAT and physical action of AgNPs.

The subcutaneous tissue compatibility of AgNP-decorated nanofilms was investigated through H&E staining, with MP-Ti as the control. Under dark conditions, after 1 day, the acute inflammatory response to the implant was observed, as indicated by the presence of vast inflammatory cell infiltration and dermal local necrosis (black arrow in Figure 10). The situation was also very serious for TA/Fe^{3+}/AgNPs-10 at 1 day postsurgery. After 4 days of implantation, no infiltration of inflammatory cells was observed, whereas a larger number of inflammatory cells (neutrophils and lymphocytes) could be observed, and the number for TA/Fe^{3+}/AgNPs-10 was much less. However, in the case of 7 days postsurgery, no neutrophils or lymphocytes were observed for TA/Fe^{3+}/AgNPs-10, whereas several inflammatory cells and mild expansion of blood vessels (red arrow) could be found in MP-Ti. With regard to the tissue section of MP-Ti irradiated with 660 nm visible light, vast inflammatory cell infiltration and dermal local necrosis were still observed similar to MP-Ti without light exposure. Furthermore, little neutrophils were observed for TA/Fe^{3+}/AgNPs-10 after illumination with 660 nm visible light. Altogether, the in vivo results reflected that the tissue reaction was much milder than that elicited by MP-Ti, especially for the PAT groups.

4. CONCLUSIONS

In summary, a thin TA/Fe^{3+}/AgNPs nanofilm was rapidly deposited onto Ti by simply mixing TA and Fe^{3+} at an ambient temperature. The quasi-spherical AgNPs were uniformly distributed into the nanofilm. Although the TA/Fe^{3+} nanofilm did not show any antibacterial activity, the AgNP-decorated nanofilms showed superior physical antibacterial activity through Ag^+ release, which increased with the increase in the initial $Ag(NH_3)_2^+$ concentration. Furthermore, the TA/Fe^{3+}/AgNPs nanofilm exhibited superior PAT efficacy when irradiated with 660 nm visible light. It should be noted that the activation of oxygen on AgNPs under such a long wavelength had rarely been reported, and a longer sensitization wavelength showed better penetrating abilities, so that it would expand the application field of AgNPs in the PAT. The high efficiency of PAT may be caused by the disruption of membrane integrity, formation of oxidative stress, and oxidative damage to key biomolecules (proteins and lipids) in bacteria. This ultrafast coating strategy proposed in this work shows superior potential in in situ rapid disinfection for implant materials.

■ ASSOCIATED CONTENT

Ⓢ Supporting Information

The Supporting Information is available free of charge on the ACS Publications website at DOI: 10.1021/acsami.7b10818.

> High-resolution SEM images of TA/Fe^{3+} Ti; surface morphology of TA/Fe^{3+}/AgNPs-10 exposed to light; EDS mapping of different elements across TA/Fe^{3+}/AgNPs-10 nanofilms; force−displacement curve of different samples detected by the nanoscratch assay; EDS spectra of TA/Fe^{3+}, TA/Fe^{3+}/AgNPs-5, and TA/Fe^{3+}/AgNPs-10; high-resolution XPS spectra of TA/Fe^{3+}, TA/Fe^{3+}/AgNPs-5, and TA/Fe^{3+}/AgNPs-10 between 700 and 740 eV; high-resolution Ag 3d XPS spectra of TA/Fe^{3+}/AgNPs-5 and TA/Fe^{3+}/AgNPs-10; depth profile of C, O, and Ag in TA/Fe^{3+}/AgNPs-10 across hybrid nanofilms; disk diffusion test for MP-Ti, TA/Fe^{3+}, TA/Fe^{3+}/AgNPs-5, and TA/Fe^{3+}/AgNPs-10; plate images of *E. coli* and *S. aureus* incubated with bare AgNPs and TA/Fe^{3+}/AgNPs-10 illuminated by 660 nm visible light; UV−vis absorbance spectra of TA/Fe^{3+}/AgNPs hybrid nanomaterials and the TA/Fe^{3+} nanofilm; and plate images of *E. coli* and *S. aureus* incubated with different samples under illumination of NIR light (PDF)

■ AUTHOR INFORMATION

Corresponding Author

*E-mail: shuilin.wu@gmail.com, shuilinwu@tju.edu.cn.

ORCID

Shuilin Wu: 0000-0002-1270-1870

Notes

The authors declare no competing financial interest.

■ ACKNOWLEDGMENTS

This work is jointly supported by the National Natural Science Foundation of China nos. 51422102, 81271715, and 21603067, the National Key Research and Development Program of China no. 2016YFC1100600 (subproject 2016YFC1100604), the Hong Kong Research Grants Council (RGC) General Research Funds (GRF) no. CityU 11301215, and the City University of Hong Kong Applied Research Grant (ARG) no. 9667144.

■ REFERENCES

(1) Konai, M. M.; Haldar, J. Lysine-Based Small Molecules that Disrupt Biofilms and Kill Both Actively Growing Planktonic and Nondividing Stationary Phase Bacteria. *ACS Infect. Dis.* **2015**, *1*, 469−478.

(2) Zhang, L.; Ning, C.; Zhou, T.; Liu, X.; Yeung, K. W. K.; Zhang, T.; Xu, Z.; Wang, X.; Wu, S.; Chu, P. K. Polymeric Nanoarchitectures on Ti-Based Implants for Antibacterial Applications. *ACS Appl. Mater. Interfaces* **2014**, *6*, 17323−17345.

(3) James, R.; Laurencin, C. T. Regenerative Engineering and Bionic Limbs. *Rare Met.* **2015**, *34*, 143−155.

(4) Zhou, T.; Zhu, Y.; Li, X.; Liu, X.; Yeung, K. W. K.; Wu, S.; Wang, X.; Cui, Z.; Yang, X.; Chu, P. K. Surface Functionalization of Biomaterials by Radical Polymerization. *Prog. Mater. Sci.* **2016**, *83*, 191−235.

(5) Wu, S.; Weng, Z.; Liu, X.; Yeung, K. W. K.; Chu, P. K. Functionalized TiO_2 Based Nanomaterials for Biomedical Applications. *Adv. Funct. Mater.* **2014**, *24*, 5464−5481.

(6) Qu, W.-T.; Sun, X.-G.; Yuan, B.-F.; Li, K.-M.; Wang, Z.-G.; Li, Y. Tribological Behaviour of Biomedical Ti−Zr-Based Shape Memory Alloys. *Rare Met.* **2017**, *36*, 478−484.

(7) Edupuganti, O. P.; Antoci, V., Jr.; King, S. B.; Jose, B.; Adams, C. S.; Parvizi, J.; Shapiro, I. M.; Zeiger, A. R.; Hickok, N. J.; Wickstrom, E. Covalent Bonding of Vancomycin to Ti_6Al_4V Alloy Pins Provides Long-Term Inhibition of Staphylococcus aureus Colonization. *Bioorg. Med. Chem. Lett.* **2007**, *17*, 2692−2696.

(8) Mei, S.; Wang, H.; Wang, W.; Tong, L.; Pan, H.; Ruan, C.; Ma, Q.; Liu, M.; Yang, H.; Zhang, L.; Cheng, Y.; Zhang, Y.; Zhao, L.; Chu, P. K. Antibacterial Effects and Biocompatibility of Titanium Surfaces with Graded Silver Incorporation in Titania Nanotubes. *Biomaterials* **2014**, *35*, 4255−4265.

(9) Zhu, P.; Weng, Z.; Li, X.; Liu, X.; Wu, S.; Yeung, K. W. K.; Wang, X.; Cui, Z.; Yang, X.; Chu, P. K. Biomedical Applications of Functionalized ZnO Nanomaterials: from Biosensors to Bioimaging. *Adv. Mater. Interfaces* **2016**, *3*, 1500494.

(10) Kazemzadeh-Narbat, M.; Kindrachuk, J.; Duan, K.; Jenssen, H.; Hancock, R. E. W.; Wang, R. Antimicrobial Peptides on Calcium Phosphate-Coated Titanium for the Prevention of Implant-Associated Infections. *Biomaterials* **2010**, *31*, 9519−9526.

(11) Zhang, F.; Zhang, Z.; Zhu, X.; Kang, E.-T.; Neoh, K.-G. Silk-Functionalized Titanium Surfaces for Enhancing Osteoblast Functions and Reducing Bacterial Adhesion. *Biomaterials* **2008**, *29*, 4751−4759.

(12) Cado, G.; Aslam, R.; Séon, L.; Garnier, T.; Fabre, R.; Parat, A.; Chassepot, A.; Voegel, J.-C.; Senger, B.; Schneider, F. Self-Defensive Biomaterial Coating Against Bacteria and Yeasts: Polysaccharide Multilayer Film with Embedded Antimicrobial Peptide. *Adv. Funct. Mater.* **2013**, *23*, 4801−4809.

(13) Gao, A.; Hang, R.; Huang, X.; Zhao, L.; Zhang, X.; Wang, L.; Tang, B.; Ma, S.; Chu, P. K. The Effects of Titania Nanotubes with

Embedded Silver Oxide Nanoparticles on Bacteria and Osteoblasts. *Biomaterials* **2014**, *35*, 4223−4235.

(14) Pazos, E.; Sleep, E.; Pérez, C. M. R.; Lee, S. S.; Tantakitti, F.; Stupp, S. I. Nucleation and Growth of Ordered Arrays of Silver Nanoparticles on Peptide Nanofibers: Hybrid Nanostructures with Antimicrobial Properties. *J. Am. Chem. Soc.* **2016**, *138*, 5507−5510.

(15) Kawata, K.; Osawa, M.; Okabe, S. In Vitro Toxicity of Silver Nanoparticles at Noncytotoxic Doses to HepG2 Human Hepatoma Cells. *Environ. Sci. Technol.* **2009**, *43*, 6046−6051.

(16) Vankayala, R.; Sagadevan, A.; Vijayaraghavan, P.; Kuo, C.-L.; Hwang, K. C. Metal Nanoparticles Sensitize the Formation of Singlet Oxygen. *Angew. Chem., Int. Ed.* **2011**, *50*, 10640−10644.

(17) Huang, Y.-F.; Zhang, M.; Zhao, L.-B.; Feng, J.-M.; Wu, D.-Y.; Ren, B.; Tian, Z.-Q. Activation of Oxygen on Gold and Silver Nanoparticles Assisted by Surface Plasmon Resonances. *Angew. Chem., Int. Ed.* **2014**, *53*, 2353−2357.

(18) Skrabalak, S. E.; Au, L.; Li, X.; Xia, Y. Facile Synthesis of Ag Nanocubes and Au Nanocages. *Nat. Protoc.* **2007**, *2*, 2182−2190.

(19) Rycenga, M.; Cobley, C. M.; Zeng, J.; Li, W.; Moran, C. H.; Zhang, Q.; Qin, D.; Xia, Y. Controlling the Synthesis and Assembly of Silver Nanostructures for Plasmonic Applications. *Chem. Rev.* **2011**, *111*, 3669−3712.

(20) Liu, K.; Liu, Y.; Yao, Y.; Yuan, H.; Wang, S.; Wang, Z.; Zhang, X. Supramolecular Photosensitizers with Enhanced Antibacterial Efficiency. *Angew. Chem., Int. Ed.* **2013**, *52*, 8285−8289.

(21) Perni, S.; Prokopovich, P.; Pratten, J.; Parkin, I. P.; Wilson, M. Nanoparticles: Their Potential Use in Antibacterial Photodynamic Therapy. *Photochem. Photobiol. Sci.* **2011**, *10*, 712−720.

(22) Ferraris, S.; Spriano, S. Antibacterial Titanium Surfaces for Medical Implants. *Mater. Sci. Eng., C* **2016**, *61*, 965−978.

(23) Liu, X.; Mou, Y.; Wu, S.; Man, H. C. Synthesis of Silver-Incorporated Hydroxyapatite Nanocomposites for Antimicrobial Implant Coatings. *Appl. Surf. Sci.* **2013**, *273*, 748−757.

(24) Jia, Z.; Xiu, P.; Li, M.; Xu, X.; Shi, Y.; Cheng, Y.; Wei, S.; Zheng, Y.; Xi, T.; Cai, H.; Liu, Z. Bioinspired Anchoring AgNPs onto Micro-Nanoporous TiO_2 Orthopedic Coatings: Trap-Killing of Bacteria, Surface-Regulated Osteoblast Functions and Host Responses. *Biomaterials* **2016**, *75*, 203−222.

(25) Zhao, C.; Feng, B.; Li, Y.; Tan, J.; Lu, X.; Weng, J. Preparation and Antibacterial Activity of Titanium Nanotubes Loaded with Ag Nanoparticles in the Dark and Under the UV light. *Appl. Surf. Sci.* **2013**, *280*, 8−14.

(26) Zhao, L.; Wang, H.; Huo, K.; Cui, L.; Zhang, W.; Ni, H.; Zhang, Y.; Wu, Z.; Chu, P. K. Antibacterial Nano-structured Titania Coating Incorporated with Silver Nanoparticles. *Biomaterials* **2011**, *32*, 5706−5716.

(27) Sanchez, C.; Arribart, H.; Guille, M. M. G. Biomimetism and Bioinspiration as Tools for the Design of Innovative Materials and Systems. *Nat. Mater.* **2005**, *4*, 277−288.

(28) Munch, E.; Launey, M. E.; Alsem, D. H.; Saiz, E.; Tomsia, A. P.; Ritchie, R. O. Tough, Bio-Inspired Hybrid Materials. *Science* **2008**, *322*, 1516−1520.

(29) Roy, X.; Hui, J. K.-H.; Rabnawaz, M.; Liu, G.; MacLachlan, M. J. Prussian Blue Nanocontainers: Selectively Permeable Hollow Metal−Organic Capsules from Block Ionomer Emulsion-Induced Assembly. *J. Am. Chem. Soc.* **2011**, *133*, 8420−8423.

(30) Li, W.; Bing, W.; Huang, S.; Ren, J.; Qu, X. Mussel Byssus-Like Reversible Metal-Chelated Supramolecular Complex Used for Dynamic Cellular Surface Engineering and Imaging. *Adv. Funct. Mater.* **2015**, *25*, 3775−3784.

(31) Ejima, H.; Richardson, J. J.; Liang, K.; Best, J. P.; van Koeverden, M. P.; Such, G. K.; Cui, J.; Caruso, F. One-Step Assembly of Coordination Complexes for Versatile Film and Particle Engineering. *Science* **2013**, *341*, 154−157.

(32) Flores, C. Y.; Diaz, C.; Rubert, A.; Benítez, G. A.; Moreno, M. S.; de Mele, M. A. F. L.; Salvarezza, R. C.; Schilardi, P. L.; Vericat, C. Spontaneous Adsorption of Silver Nanoparticles on Ti/TiO_2 Surfaces. Antibacterial Effect on Pseudomonas aeruginosa. *J. Colloid Interface Sci.* **2010**, *350*, 402−408.

(33) Shen, H.; Duan, C.; Guo, J.; Zhao, N.; Xu, J. Facile In Situ Synthesis of Silver Nanoparticles on Boron Nitride Nanosheets with Enhanced Catalytic Performance. *J. Mater. Chem. A* **2015**, *3*, 16663−16669.

(34) Rainville, L.; Dorais, M.-C.; Boudreau, D. Controlled synthesis of low polydispersity Ag@SiO_2 core−shell nanoparticles for use in plasmonic applications. *RSC Adv.* **2013**, *3*, 13953−13960.

(35) Fan, W.; Huang, P.; Chen, X. Overcoming the Achilles' heel of Photodynamic Therapy. *Chem. Soc. Rev.* **2016**, *45*, 6488−6519.

(36) Li, M.; Liu, X.; Xu, Z.; Yeung, K. W. K.; Wu, S. Dopamine Modified Organic−Inorganic Hybrid Coating for Antimicrobial and Osteogenesis. *ACS Appl. Mater. Interfaces* **2016**, *8*, 33972−33981.

(37) Lu, Z.; Li, C. M.; Bao, H.; Qiao, Y.; Toh, Y.; Yang, X. Mechanism of Antimicrobial Activity of CdTe Quantum Dots. *Langmuir* **2008**, *24*, 5445−5452.

(38) Ye, Q.; Zhou, F.; Liu, W. Bioinspired Catecholic Chemistry for Surface Modification. *Chem. Soc. Rev.* **2011**, *40*, 4244−4258.

(39) Wang, G.; Jin, W.; Qasim, A. M.; Gao, A.; Peng, X.; Li, W.; Feng, H.; Chu, P. K. Antibacterial Effects of Titanium Embedded with Silver Nanoparticles Based on Electron-Transfer-Induced Reactive Oxygen Species. *Biomaterials* **2017**, *124*, 25−34.

(40) Piantanida, G.; Menart, E.; Bicchieri, M.; Strlič, M. Classification of Iron-Based Inks by Means of Micro-Raman Spectroscopy and Multivariate Data Analysis. *J. Raman Spectrosc.* **2013**, *44*, 1299−1305.

(41) Zaleski, S.; Wilson, A. J.; Mattei, M.; Chen, X.; Goubert, G.; Cardinal, M. F.; Willets, K. A.; Van Duyne, R. P. Investigating Nanoscale Electrochemistry with Surface- and Tip-Enhanced Raman Spectroscopy. *Acc. Chem. Res.* **2016**, *49*, 2023−2030.

(42) Jin, J.-C.; Xu, Z.-Q.; Dong, P.; Lai, L.; Lan, J.-Y.; Jiang, F.-L.; Liu, Y. One-Step Synthesis of Silver Nanoparticles Using Carbon Dots as Reducing and Stabilizing Agents and Their Antibacterial Mechanisms. *Carbon* **2015**, *94*, 129−141.

(43) Wang, Q.; Zhang, Y.; Yang, K.; Tan, L. Preparation of Bioactive Film on Ti_6Al_4V. *Surf. Rev. Lett.* **2009**, *16*, 775−779.

(44) Lee, J. S.; Murphy, W. L. Functionalizing Calcium Phosphate Biomaterials with Antibacterial Silver Particles. *Adv. Mater.* **2013**, *25*, 1173−1179.

(45) Ritger, P. L.; Peppas, N. A. A Simple Equation for Description of Solute Release II. Fickian and Anomalous Release from Swellable Devices. *J. Controlled Release* **1987**, *5*, 37−42.

(46) Silva, F. M.; Pinto, R. J. B.; Daniel-da-Silva, A. L.; Trindade, T. Cationic Release Behaviour of Antimicrobial Cellulose/Silver Nanocomposites. *Cellulose* **2014**, *21*, 3551−3560.

(47) Xiu, Z.-m.; Zhang, Q.-b.; Puppala, H. L.; Colvin, V. L.; Alvarez, P. J. J. Negligible Particle-Specific Antibacterial Activity of Silver Nanoparticles. *Nano Lett.* **2012**, *12*, 4271−4275.

(48) Liu, J.; Sonshine, D. A.; Shervani, S.; Hurt, R. H. Controlled Release of Biologically Active Silver from Nanosilver Surfaces. *ACS Nano* **2010**, *4*, 6903−6913.

(49) Creutz, C.; Brunschwig, B. S.; Sutin, N. Interfacial Charge-Transfer Absorption: Semiclassical Treatment. *J. Phys. Chem. B* **2005**, *109*, 10251−10260.

(50) Li, Y.; Zhang, W.; Niu, J.; Chen, Y. Mechanism of Photogenerated Reactive Oxygen Species and Correlation with the Antibacterial Properties of Engineered Metal-Oxide Nanoparticles. *ACS Nano* **2012**, *6*, 5164−5173.

(51) Xu, Z.; Li, M.; Li, X.; Liu, X.; Ma, F.; Wu, S.; Yeung, K. W. K.; Han, Y.; Chu, P. K. Antibacterial Activity of Silver Doped Titanate Nanowires on Ti Implants. *ACS Appl. Mater. Interfaces* **2016**, *8*, 16584−16594.

(52) Zhou, P.; Xia, Y.; Cheng, X.; Wang, P.; Xie, Y.; Xu, S. Enhanced Bone Tissue Regeneration by Antibacterial and Osteoinductive Silica-HACC-zein Composite Scaffolds Loaded with rhBMP-2. *Biomaterials* **2014**, *35*, 10033−10045.

(53) Choi, B.-H.; Choi, Y. S.; Kang, D. G.; Kim, B. J.; Song, Y. H.; Cha, H. J. Cell Behavior on Extracellular Matrix Mimic Materials Based on Mussel Adhesive Protein Fused with Functional Peptides. *Biomaterials* **2010**, *31*, 8980−8988.

(54) Oh, S.; Brammer, K. S.; Li, Y. S. J.; Teng, D.; Engler, A. J.; Chien, S.; Jin, S. Stem Cell Fate Dictated Solely by Altered Nanotube Dimension. *Proc. Natl. Acad. Sci. U.S.A.* **2009**, *106*, 2130−2135.

Supporting Information

Tannic Acid/Fe^{3+}/Ag Nanofilm Exhibiting Superior Photodynamic and Physical Antibacterial Activity

Ziqiang Xu[a], Xiuhua Wang[a], Xiangmei Liu[a], Zhenduo Cui[b], Xianjin Yang[b], Kelvin Wai Kwok Yeung[d], Jonathan Chiyuen Chung[c], Paul K. Chu[c], Shuilin Wu[a,b]*

[a] *Hubei Collaborative Innovation Center for Advanced Organic Chemical Materials, Ministry-of-Education Key Laboratory for the Green Preparation and Application of Functional Materials, Hubei Key Laboratory of Polymer Materials, School of Materials Science & Engineering, Hubei University, Wuhan 430062, China*

[b] *School of Materials Science & Engineering, Tianjin University, Tianjin 300072, China*

[c] *Department of Physics and Department of Materials Science and Engineering, City University of Hong Kong, Tat Chee Avenue, Kowloon, Hong Kong, China*

[d] *Department of Orthopaedics & Traumatology, Li Ka Shing Faculty of Medicine, The University of Hong Kong, Pokfulam, Hong Kong, China*

* *To whom correspondence should be addressed:*

E-mail: shuilin.wu@gmail.com; shuilinwu@tju.edu.cn (S.L. Wu)

Table of contents

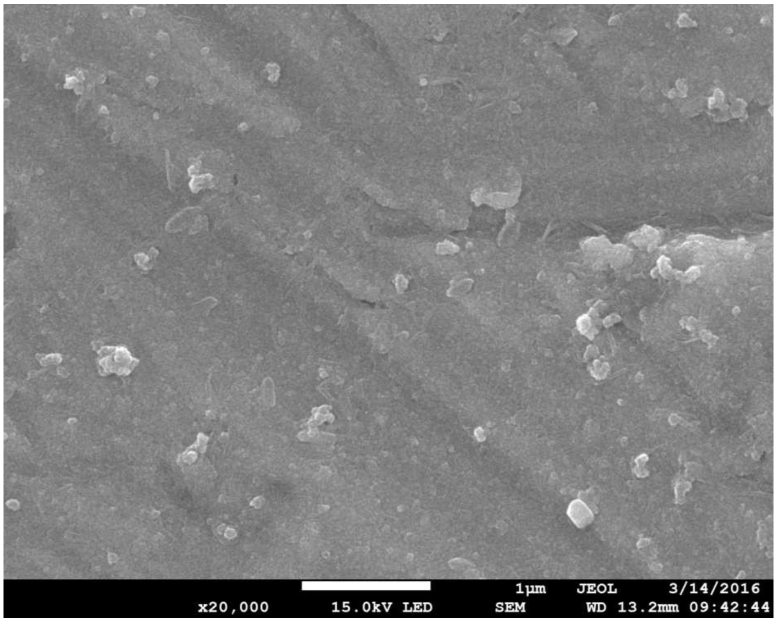

Figure S1

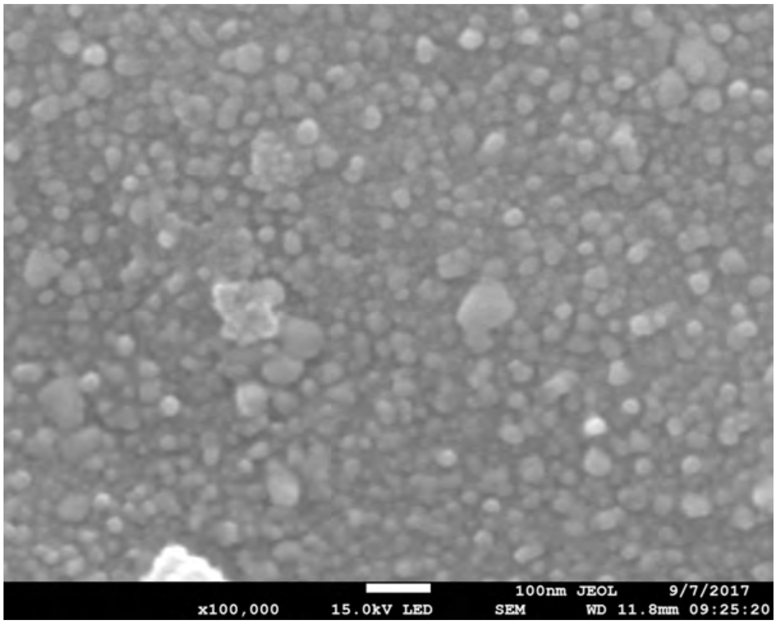

Figure S2

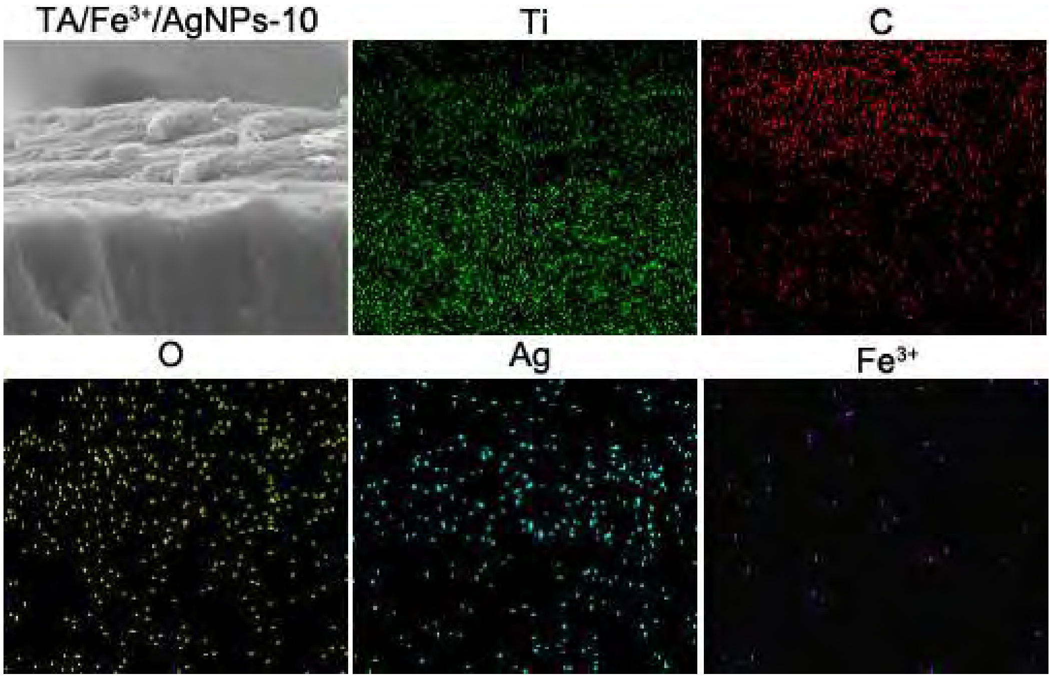

Figure S3

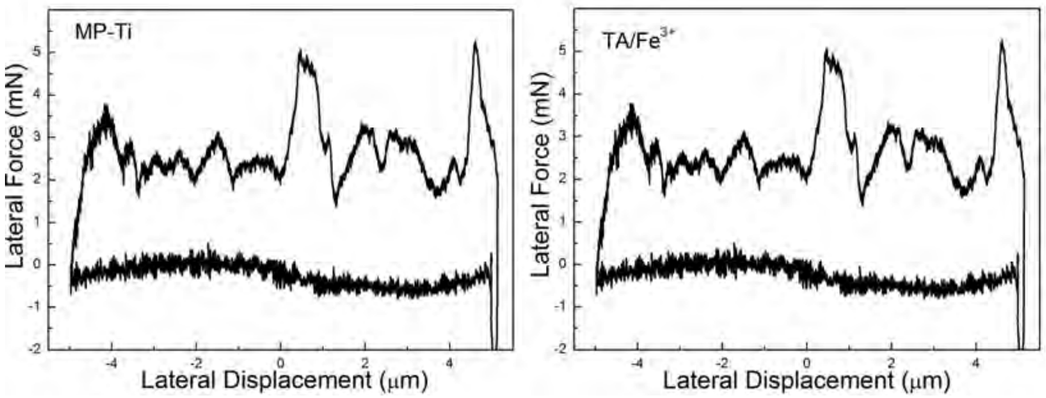
MP-Ti
TA/Fe^{3+}
Lateral Force (mN)
Lateral Displacement (μm)
-2
-1
0
1
2
3
4
5
-4
-2
0
2
4

Figure S4

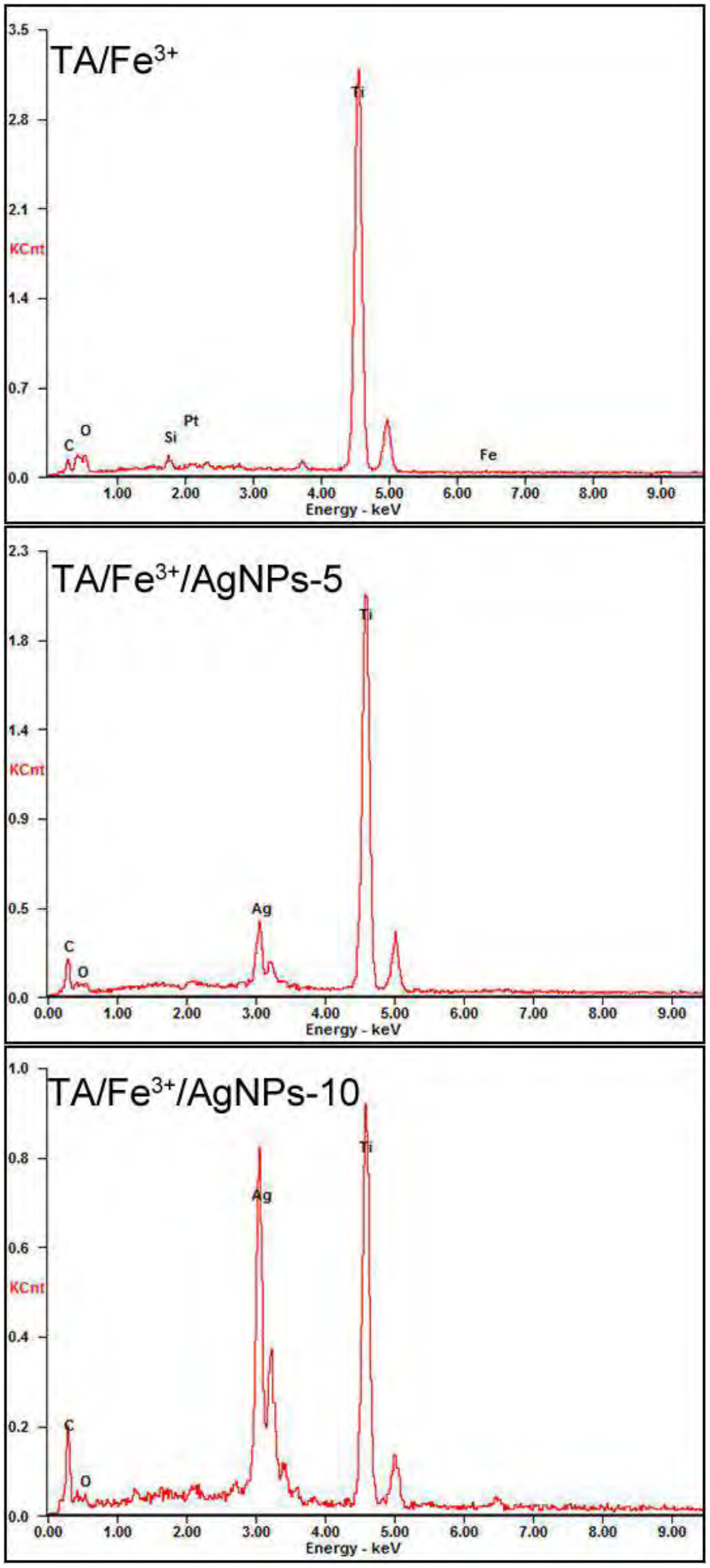
TA/Fe3+
3.5
2.8
2.1
KCnt
1.4
0.7
0.0
C
O
Si
Pt
Ti
Fe
1.00
2.00
3.00
4.00
5.00
6.00
7.00
8.00
9.00
Energy - keV
TA/Fe3+/AgNPs-5
2.3
1.8
1.4
KCnt
0.9
0.5
0.0
C
O
Ag
Ti
0.00
1.00
2.00
3.00
4.00
5.00
6.00
7.00
8.00
9.00
Energy - keV
TA/Fe3+/AgNPs-10
1.0
0.8
0.6
KCnt
0.4
0.2
0.0
C
O
Ag
Ti
0.00
1.00
2.00
3.00
4.00
5.00
6.00
7.00
8.00
9.00
Energy - keV

Figure S5

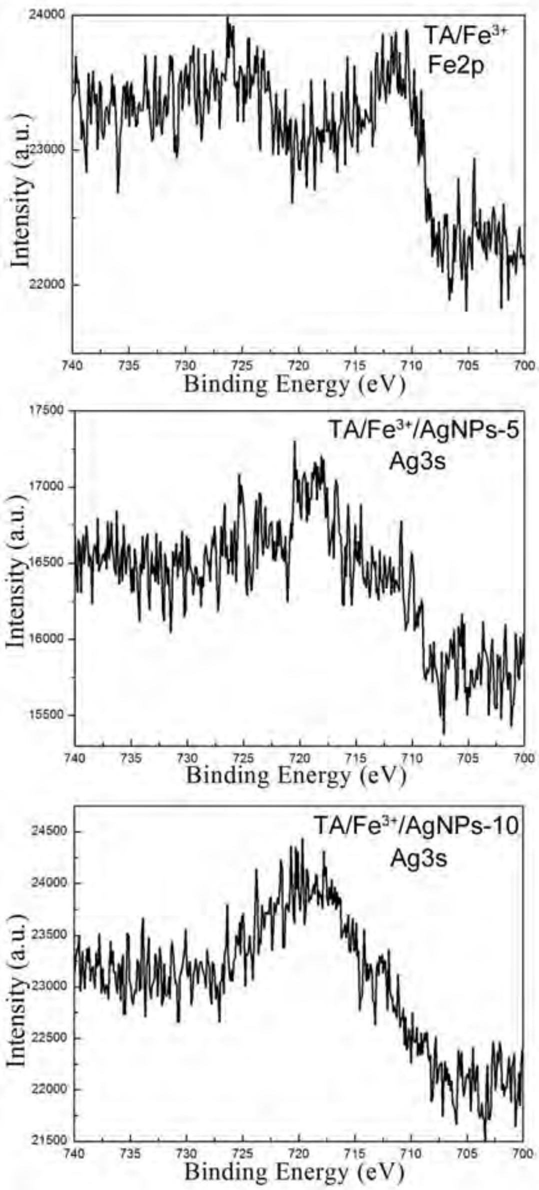
TA/Fe³⁺
Fe2p
Intensity (a.u.)
24000
23000
22000
740
735
730
725
720
715
710
705
700
Binding Energy (eV)
TA/Fe³⁺/AgNPs-5
Ag3s
17500
17000
16500
16000
15500
TA/Fe³⁺/AgNPs-10
Ag3s
24500
24000
23500
23000
22500
22000
21500

Figure S6

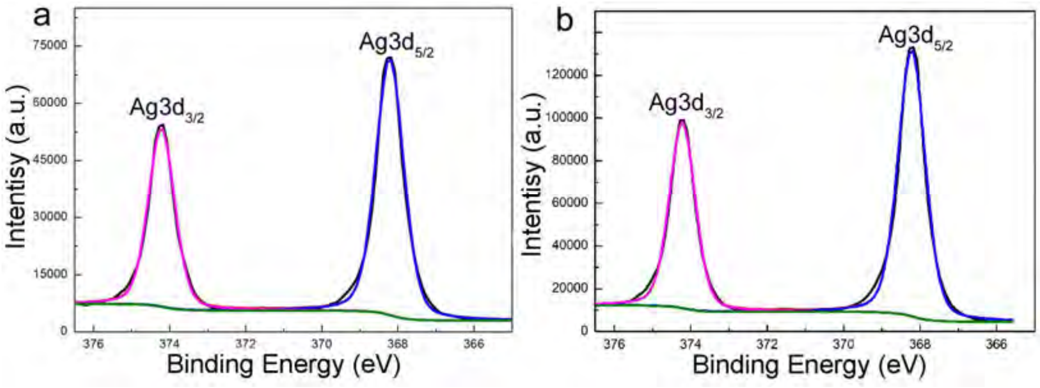
a
Ag3d3/2
Ag3d5/2
Intentisy (a.u.)
75000
60000
45000
30000
15000
0
376
374
372
370
368
366
Binding Energy (eV)
b
Ag3d3/2
Ag3d5/2
Intentisy (a.u.)
120000
100000
80000
60000
40000
20000
0
376
374
372
370
368
366
Binding Energy (eV)

Figure S7

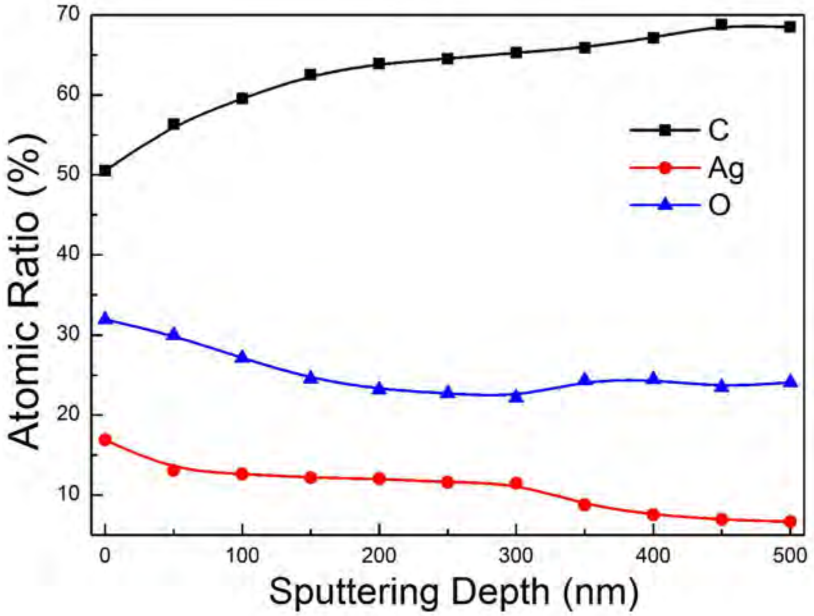

Atomic Ratio (%)
70
60
50
40
30
20
10
0
100
200
300
400
500
Sputtering Depth (nm)
C
Ag
O

Figure S8

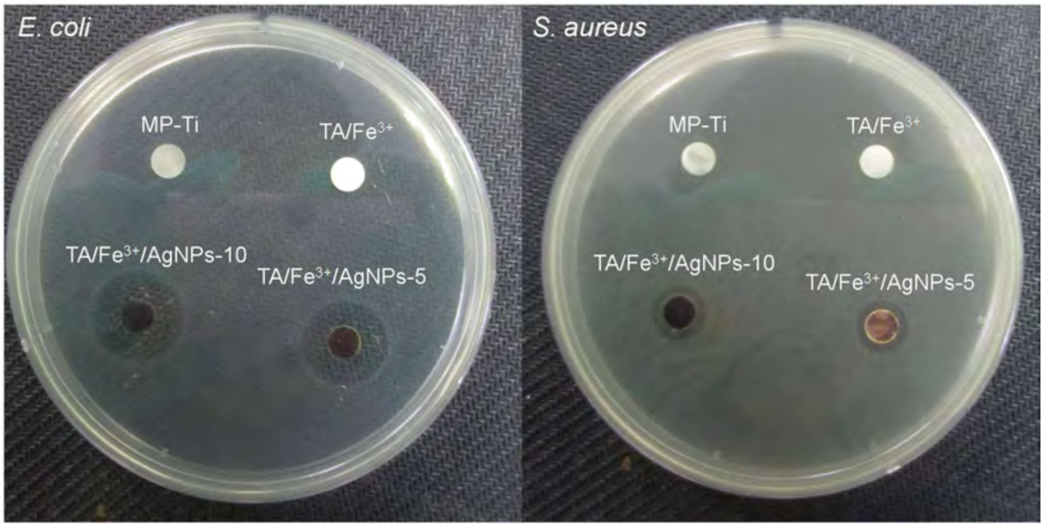
E. coli
MP-Ti
TA/Fe3+
TA/Fe3+/AgNPs-10
TA/Fe3+/AgNPs-5
S. aureus
MP-Ti
TA/Fe3+
TA/Fe3+/AgNPs-10
TA/Fe3+/AgNPs-5

Figure S9

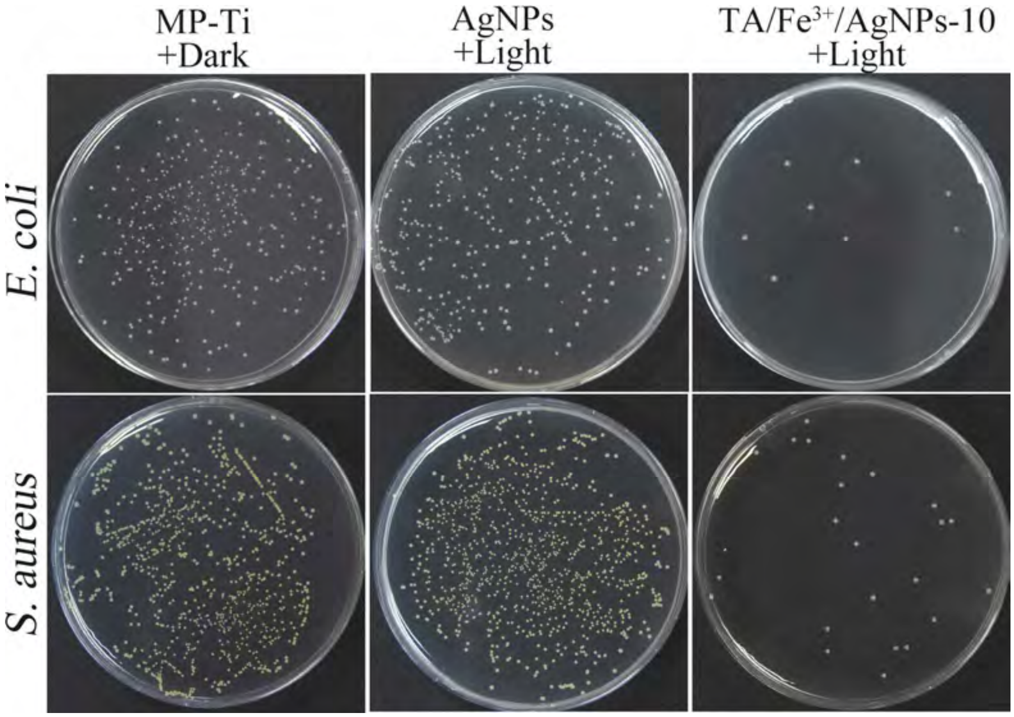

Figure S10

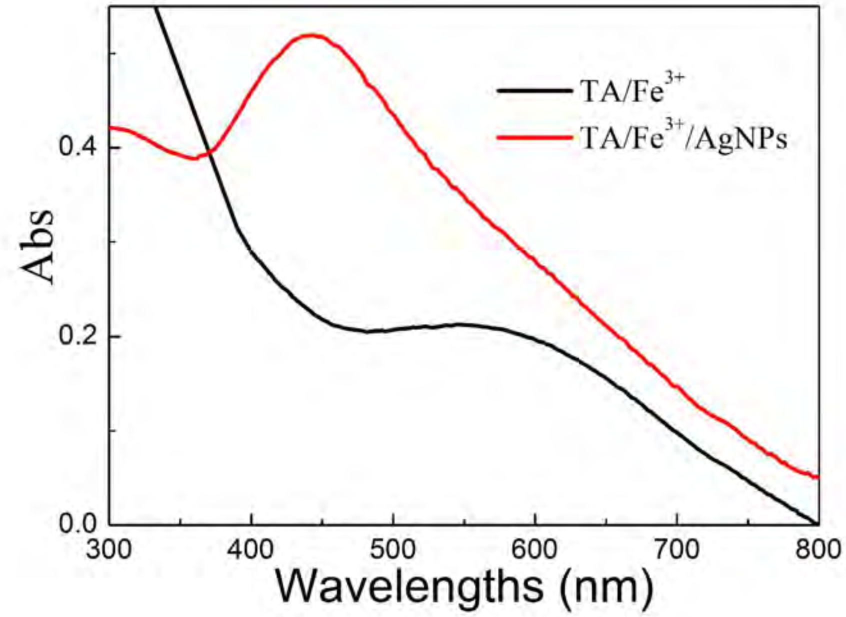

TA/Fe^{3+}
TA/Fe^{3+}/AgNPs
Abs
0.0
0.2
0.4
300
400
500
600
700
800
Wavelengths (nm)

Figure S11

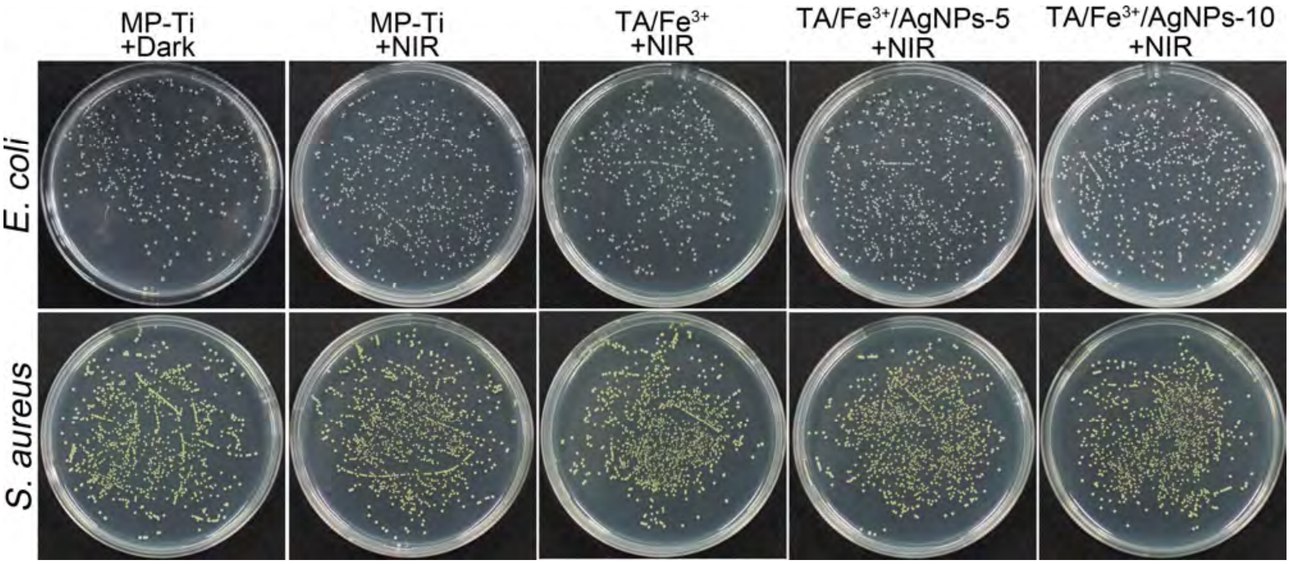
MP-Ti
+Dark
MP-Ti
+NIR
TA/Fe3+
+NIR
TA/Fe3+/AgNPs-5
+NIR
TA/Fe3+/AgNPs-10
+NIR
E. coli
S. aureus

Figure S12